Microjet Angle Sensitivity for Active Flow Control on Multi-Element High-Lift Systems

James R. L. Koch*, Jeffrey A. Housman†, and Seyedeh Sheida Hosseini‡
NASA Ames Research Center, Moffett Field, CA 94035

This paper concerns the modeling and analysis of angled active flow control microjets using Computational Fluid Dynamics (CFD). Two geometries are considered: a 2D NLR7301 two-element airfoil with 20° flap deflection, and a 3D Common Research Model in a high lift configuration (CRM-HL) with inboard and outboard flaps deflected 40° and 37°, respectively. An overset grid system representing the NLR7301 is generated and microjets with a width of 0.5% of the wing chord are placed on the pressure and suction sides of the NLR flap at 95% of the flap chord. A code-to-code comparison against published CFD solutions is presented for a normal-blowing pressure-side jet for momentum coefficient range of $0.0004 < C_\mu < 0.04$. A case matrix is then run for the same range of C_μ values over a range of jet angles θ (30° off the flap surface upstream of the microjet to 30° off the downstream flap surface), and the trends are discussed. Subsequently, a jet trade-off study is then performed for the NLR7301 in which pressure-side normal and suction-side tangent jets are compared individually and in tandem. The overset grid system representing the CRM-HL geometry is borrowed from the LAVA entry of the 4th AIAA High Lift Prediction Workshop (HLPW4). Microjets with a width of 0.5% of the mean aerodynamic chord are implemented on the inboard flap at 95% and 4.75% of the flap chord on the pressure and suction sides, respectively. Jet-off solutions are shown to match those reported in the HLPW4, after which two studies are performed: a single pressure-side jet angle sweep is performed for a C_μ of 0.00278, and a pressure-suction jet trade-off study similar to that performed for the NLR7301. Findings indicate that for system analysis-relevant C_μ values, there exists a range of microjet angles local to normal-blowing for which optimal induced aerodynamic coefficient deltas remain effectively constant. For the 2D NLR7301 drag is significantly influenced by jet momentum, while for the 3D CRM-HL pressure drag changes overshadows it. When comparing pressure-side normal-blowing and suction-side tangent-blowing jets, both normal, tangent, and tandem blowing increases lift as long as the tandem jets are strong enough. Drag is reduced for all NLR7301 jet configurations of the trade-off study, while for the CRM-HL it is increased by normal blowing. All NLR7301 simulations presented were computed using the Unsteady Reynolds-averaged Navier-Stokes (URANS) equations, while the CRM-HL cases were computed using RANS.

I. Introduction

The paper concerns small jets integrated into an airfoil known as 'microjets'; one of the active flow control (AFC) methods which has garnered interest in recent years. One of the purviews of AFC is efficiency and aerodynamic control of high-lift systems. High-lift systems have been both a challenging and integral task for the civil transport industry because they dictate payload limits as well as take-off and landing distances and speeds.[1–3] The higher the maximum lift coefficient, the smaller airplane wings need to be and the lower cruise drag will be. For configurations such as twin-engines, engine-out climb requirements are directly related to lift-to-drag ratio at takeoff. Similarly, the required tail ground clearance angle dictates the needed lift coefficient for a given angle of attack (AOA). Meredith summed up these interrelated requirements when concluding that a "0.10 increase of lift coefficient at constant AOA is equivalent to reducing the approach attitude by one degree.", which translates to in a potential savings in airplane weight of 1400

*Computational Aerosciences Branch, AIAA Member, james.r.koch@nasa.gov
†Computational Aerosciences Branch, AIAA Senior Member, jeffrey.a.housman@nasa.gov
‡Computational Aerosciences Branch, AIAA Member, seyedeh.sheida.hosseini@nasa.gov

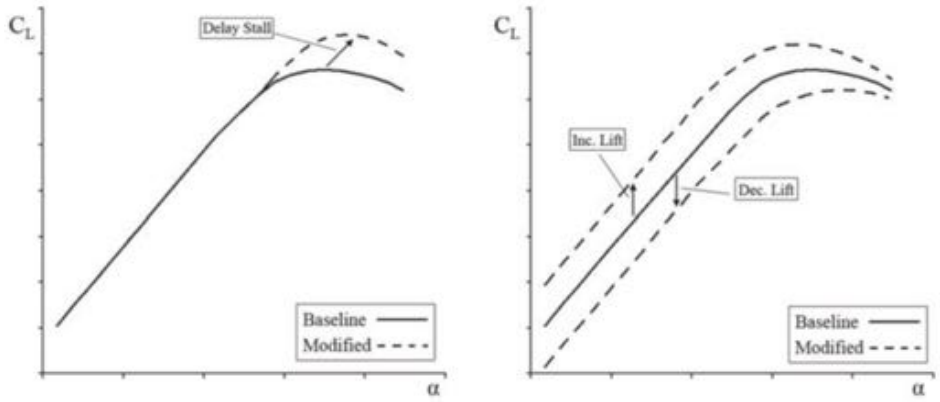

Figure 1. Lift coefficient C_l for an AOA sweep. (*Left*): Separation mitigation through increase of attainable maximum lift. (*Right*): Aerodynamic load control through vertical shifting of lift curve. (Taken from Johnson et al.[26]).

lbs.[4] While current high-lift systems have been designed to achieve desired performance with simplicity in mind (reduced flap elements, fixed flap hinges, etc.), there remain very few possibilities to further improve performance through physical alteration of the airfoils themselves. AFC technology thus seeks to increase the performance of high-lift systems in some desired way through influencing the aerodynamic characteristics of the system's slow-acting airfoils such as flaps in a fast-acting manner.

AFC can be designed to address a variety of aerodynamic challenges, with two of the most important being separation mitigation and load control. As depicted in Figure 1, the former pertains to increasing the maximum attainable lift coefficient C_l (correlating to stall prevention which allows deeper flap deflection), while the latter pertains to shifting the linear region of the C_l curve. Until recently, most pneumatic AFC technologies blew a jet tangent to the free-stream, being placed either upstream of the flap,[5] near the flap leading edge,[6,7] or at the trailing edge of flaps utilizing the Coanda effect.[8–10] In contrast, the newly considered normal-blowing microjets are small, pneumatic jets pointing perpendicular to the airfoil surface often placed near the trailing edge of single-element[11–21] or multi-element[22–25] airfoils to induce significant circulation control and change in aerodynamic performance while requiring a relatively small air pressure and flow rate. From an aerodynamic perspective, increasing lift correlates to moving toward the inviscid limits of the system: a completely inviscid flow achieves maximum theoretical lift. Tangent-blowing jets seek to increase lift by injecting momentum energy into the boundary layer in the stream-wise direction local to adverse pressure gradients on an airfoil (often on the suction side) which separate the flow. By changing the pressure field around the airfoil, tangent jets can also take advantage of the Coanda effect to effectively change the effective shape (i.e. camber) of the airfoil by the flow. This induced by the change in airfoil shape is independent of the inviscid limits of the system, and has been recognized as having high potential for 'circulation control'. Microjets which blow normal to the surface tend to affect their systems significantly only through change in pressure field and thus airfoil shape and circulation.

There are several important parameters which affect the performance of microjets, including width, chordwise location, and jet strength. The effect of these has been examined in detail for the two geometries considered in this work due to availability of experimental and Computational Fluid Dynamics (CFD) data in the literature: the multi-element NLR7301 airfoil,[27] chosen due to experimental benchmark availability,[22–25] and the High-Lift Common Research Model[28] (CRM-HL) used for various AIAA High Lift Prediction Workshops.[29–31] This work concerns a jet parameter which has not been considered by the aforementioned literature: the angle of the microjet relative to the airfoil surface. CFD has found that normal-blowing near the trailing edge can reliably modify the pressure distribution to achieve lift control,[22–25] and results compare well against an experiment performed by Malavard[11] for which a microjet was blowing at 90 degrees. However, it is not reasonable to assume that construction of the microjet plenum will always guarantee an exit angle of 90 degrees to the aerofoil surface because of feasibility constraints related to thin trailing edge thicknesses. Studies are therefore conducted to ascertain under what jet angle tolerance normal-blowing conditions can be assumed. Studies are also performed to assess how the more traditional suction-side tangent-blowing microjet strategy compares to its newer pressure-side normal-blowing counterpart by looking at their influence on the effective chord and camber of the airfoil due to alterations in the pressure field and aerodynamic force coefficients.

The structure of this paper is as follows. The Launch, Ascent, and Vehicle Aerodynamics (LAVA) CFD framework chosen for this work is described in Section II, along with the methodology behind overset gridding. Following this, the implementation of boundary conditions representing angled microjets is discussed in Section III. Microjets are then introduced into the NLR7301 multi-element airfoil to verify their implementation and explore the effect of jet angle. Best practices for simulating the NLR7301 using LAVA are defined in Section IV, which include gridding (Section IV.A), solver settings such as turbulence model and convection scheme (Section IV.B), grid resolution (Section IV.C), and solution validation/code-to-code comparison (Sections IV.D and IV.E). These best practices are then used to conduct a series of jet angle sweeps at various jet strengths in Section V, first looking at the methodology behind picking jet parameters (Section V.A), then investigating the interrelation of pressure-side jet strength and angle (Section V.B), the effect of significantly increasing pressure-side angled jet strength (Section V.C), and the trade-off of using pressure-side normal-blowing and/or suction-side tangent-blowing microjets (Section V.D). Microjets are then added onto the inboard flap of the LAVA grid system used for the 4th AIAA High Lift Prediction Workshop's CRM-HL. An overview of the found best practices used to simulate the CRM-HL with LAVA are discussed in Section VI, along with a jets-off solution. Two angled jet studies are then performed in Section VII emulating those performed on the NLR7301: a pressure-side jet angled sweep (Section VII.A), and a pressure-side normal-blowing and/or suction-side tangent-blowing jet trade-off study (Section VII.B).

II. Computational Methodology

This work utilizes the Launch, Ascent, and Vehicle Aerodynamics (LAVA) framework, which can simulate complex geometries for a broad range of aerospace applications and allows for several mesh paradigms.[32,33] The mesh paradigm chosen in this work is the structured curvilinear overset grid method, representing the computational domain with overlapping, body-fitted curvilinear meshes. Overset gridding is a manual and potentially time-intensive process, but allows extensive grid manipulation and tailoring, even for arbitrarily complex technologies. When building a computational domain with this method, surface or volume grids are drawn onto or built from the surface of the CAD geometry, and volumes are then hyperbolically grown from the surfaces and moved using scripted commands native to the Chimera Grid Tools software package.[34] Within an overset framework, where singular grids have no known knowledge of the modeled geometry as a whole, portions of them may fall outside the computational domain and are therefore omitted from the set of utilized computational nodes (i.e. blanked) using the 'implicit' hole cutting (IHC) algorithms native to the LAVA Curvilinear solver in which the true surface of the computational domain manifold is implicitly determined by surface projection and in-out test ray-casting.[35] Grids must overlap by a computational stencil's worth of fringe nodes or proper communication between grids cannot occur and 'orphans', i.e., nodes which (as per the requirements of the LAVA solver) do not overlap with non-fringe nodes, are formed. After a minimum connection is achieved through IHC, grid overlap is optimized by further blanking grid nodes when an overlap stencil exists with more similar cell sizes and orientations.[35] For a description of the overset grid system representing the computational domain of the NLR7301 geometry, see Section IV.A.

The LAVA curvilinear solver can solve the Reynolds-Averaged Navier-Stokes (RANS) equations using any of several methods coded into the LAVA framework. LAVA's linear solver uses an incomplete lower-upper factorization with a user-prescribed level of fill (in this case zero). This preconditions the Krylov-subspace linear solver generalized minimal residual method.[36] A hybrid Message Passing Interface/OpenMP parallelization strategy is also used, where all of the numerically intensive routines have been vectorized. Local pseudo-time stepping also accelerates nonlinear convergence with a self-ramping pseudo-time CFL. Finally, tiling is used to replace physical domain decomposition in order to enable a scalable well-balanced parallel domain decomposition. For a description of the numerical methods used to discretize the RANS equations, and turbulence model chosen when simulating the NLR7301, see Section IV.B.

III. Implementation of Jet Boundary Conditions

The effect that the microjets have on a flow field can be described in terms of how much force due to momentum they introduce, and are thus commonly characterized by the coefficient of momentum $C_{\mu,jet}$ shown in Equation 1. This coefficient represents the normalized momentum force exiting from the microjet nozzle or plenum into the free-stream. The area of the jet A_{jet}, defined in Equation 2 and visualized in Figure 2, represents the cross-sectional area of the jet as seen from the n_{jet} direction of flow as it exits the

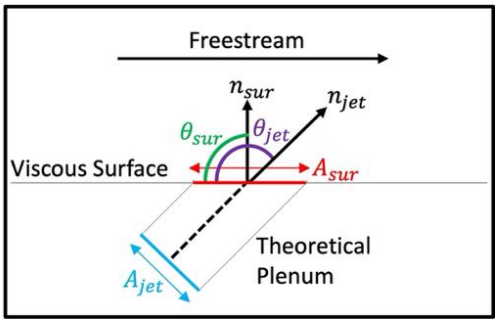

Figure 2. Visual example of calculating jet area A_{jet} for a jet placed on a viscous aerodynamic surface based on jet angle θ_{jet} and resulting jet normal n_{jet}. n_{sur} is the average normal of the surface on which the jet is defined. The area of the surface on which the jet is defined A_{sur} is projected onto a theoretical plenum along n_{jet} in order to find the effective exit area A_{jet}. If the jet was blowing normal to the surface, $n_{jet} \rightarrow n_{sur}$ and $A_{jet} \rightarrow A_{sur}$ via Equation 2.

nozzle. This becomes important for CFD simulations, as often boundary conditions (BCs) which represent these microjets are implemented on a surface with normal n_{sur} without modeling the nozzle or plenum providing the injected flow. Thus, the term $n_{sur} \cdot n_{jet}$ must be included in case the surface and jet direction are not aligned in order to account for the difference in effective exit area A_{jet}. In this work, a jet's angle is measured from the upstream surface the jet is being placed on. For a locally flat plate, n_{sur} would correspond to θ_{jet} of 90.

A visual example of the effect jet angle can have on jet area by projecting it to a 'theoretical' planar plenum is also shown in Figure 2. Jets on the surface of aerodynamic bodies will necessarily introduce an aerodynamic force on the body onto which it is placed due to the momentum of the fluid it is expelling. The components i of this momentum coefficient may be calculated analytically using Equation 1 multiplied by $-n_{jet_i}$, and subsequently transformed into lift and drag contributions. It is important to note that the angled jet BCs in this work assume a theoretical plenum in lieu of knowing what shape the plenum is. Modeling any plenum will introduce an effective change in jet angle due to flow entrainment within the plenum, and may cause plenum-dependent shifts in the trends presented in the following sections. Plenums which could be manipulated to alter jet angle may also have more restrictive angle limits than those explored in this work, especially if located close to the trailing edge, due to geometric restrictions.

$$C_{\mu,jet} = \frac{2\rho_{jet} A_{jet} U_{jet}^2}{\rho_\infty A_\infty U_\infty^2} \tag{1}$$

$$A_{jet} = A_{sur} * (n_{sur} \cdot n_{jet}) \tag{2}$$

In CFD, subsonic inflow BCs require two of the three primitive variables (pressure p, the vector of the three velocity components $\vec{U}$, and temperature T) to be defined, with the third being interpolated from the interior of the computational domain. To specify a boundary condition using Equation 1, two of three unknown parameters $(\rho_{jet}, U_{jet}, C_{\mu,jet})$ must be provided, and the jet angle relative to the surface it is imposed on must be specified. In recent publications concerning 'normal-blowing' microjets, two main assumptions were made: firstly, incompressibility was assumed (i.e., $\rho_{jet} = \rho_\infty$), and secondly, flow exited the jet normal to the surface (i,e,. $(n_{sur} \cdot n_{jet}) = 1$).[22–25] This results in a boundary condition for which the jet velocity magnitude U_{jet} could either be defined or inferred directly from $C_{\mu,jet}$. Thus, since $n_{sur} = n_{jet}$, $\vec{U}$ can be set from U_{jet} and n_{sur}, T is set to T_∞, and p is interpolated. To define an angled jet, these previous assumptions of incompressibility and surface-normal jet flow cannot be made because now $\vec{U}$ is explicitly defined from U_{jet} and n_{jet}, p is interpolated, and T is inferred from ρ_{jet} using the isentropic relation based on the assumption of an ideal gas defined in Equation 3. In order to use Equation 1 ρ_{jet} can no longer be omitted as an unknown parameter: if it is not defined, both $C_{\mu,jet}$ and U_{jet} must be provided.

$$T_{jet} = \frac{p_{jet}}{R_{gas}\rho_{jet}} \tag{3}$$

The mass flow rate $\dot{m}$ can be pulled from Equation 1 to form Equation 4a, which in many ways is preferable as $\dot{m}$ is a more 'engineering-friendly' term from the perspective of design. There is a fundamental difference between using Equation 1 and Equation 4a, however: when using the latter, the three unknown parameters now become $\dot{m}_{jet}$, U_{jet} and $C_{\mu,jet}$, i.e., the mass parameter defined by the user changes from

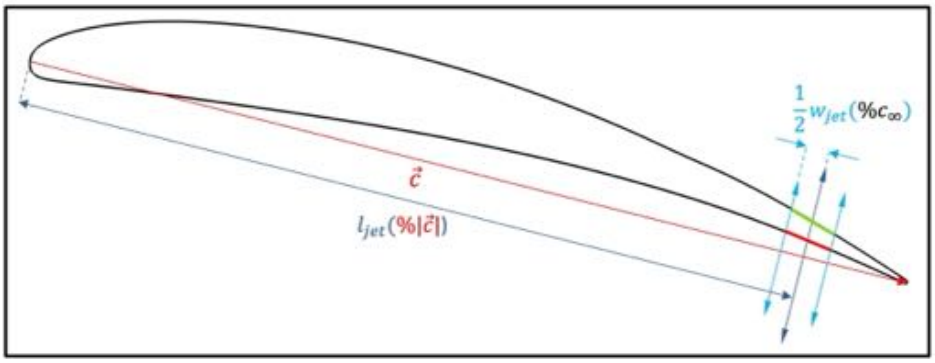

Figure 3. Visual example of constructing a jet on the surface of an airfoil. l_{jet} is location of the jet center along the chord and w_{jet} is the width of the jet. The chord vector ($\vec{c}$)-normal rays cast at the limits of the chord jet define the limits of the airfoil-surface jet where they intersect. Example jets inscribed on the pressure and suction side of the airfoil using this method are shown in red and green, respectively.

ρ_{jet} to $\dot{m}_{jet}$. Because ρ_{jet} must still be provided, it must be solved for in Equation 4b, meaning that the third unknown of the BC must be found using Equation 4a. Compared to the density-related version of the momentum coefficient Equation 1 the velocity magnitude U_{jet} is reduced by a power, requiring careful consideration of $\dot{m}_{jet}$ if two jets using the different formulations are to be comparable.

$$C_{\mu,jet} = \frac{2 * \dot{m}_{jet} * U_{jet}}{\dot{m}_\infty * U_\infty} \tag{4a}$$

$$\dot{m}_{jet} = \rho_{jet} * A_{jet} * U_{jet} \tag{4b}$$

$$\dot{m}_\infty = \rho_\infty * A_\infty * U_\infty \tag{4c}$$

When defining jets on the surfaces of airfoils (flaps in the case of this work), the following strategy depicted in Figure 3 is used. For a given cross-section of the airfoil, the chord vector $\vec{c}$ is drawn from the leading edge to the center of the trailing edge. The location along $\vec{c}$ at which the jet will be centered, l_{jet}, is measured from the leading edge and is defined as a percentage of the airfoil chord length. The width of the jet w_{jet} is measured outward from l_{jet} and is defined as a percentage of the reference wing chord c_∞. To find the limits of the jet on the airfoil surface, rays are cast perpendicularly at the limits of the jet along $\vec{c}$ and their intersection with the airfoil geometry is tagged. The jet can then be constructed on the airfoil surface.

IV. Best Practices for Simulating the NLR7301 with LAVA Curvilinear

The NLR7301 multi-element airfoil geometry was chosen to be simulated because it is a good two dimensional representation of the commercial wings high-lift systems AFC microjets are being considered for, and published data from both benchmark experiments[27] and CFD using OVERFLOW best practices[25] exists to compare against. An overview of the NLR7301 geometry, as well as the best practices developed for representing its computational domain with overset curvilinear grids is presented in Section IV.A. This is followed by an explanation of the strategy used to simulate this grid system in Section IV.B. Finally, a set of studies is performed to a) bound the discretization-related uncertainty of the grid system via a refinement study (Section IV.C), b) validate the solution accuracy against published experimental data when no microjets are included (Section IV.D), and c) perform a code-to-code comparison against published CFD data for normal-blowing microjets on the pressure side (Section IV.E).

IV.A. Overset Gridding Best Practices for Simulating the NLR7301

The NLR7301 geometry and overset grid system comprising its computational domain are shown in Figure 4. The flap is deflected at 20.0°, which corresponds to a gap and overlap reported to be 2.6% and 5.3% of the cruise chord, respectively.[27] The wing and flap have body-fitted grids on their surface, with an H-topology grid strategy being adopted at the trailing edges to allow gradients of flow turning the trailing edge corners to be properly resolved. The body-fitted grids of the flap are grown to a fixed width, and then coarsened so that all body-fitted grids cleanly interface with their local off-body grids. Wake grids are placed at the

trailing edges of both elements. For the wing, this allows for resolution of the shear layer coming off of the wing, which can then continue to be captured within the fine flap body-fitted grids. For the flap, the wake is uniform and fine, growing out to the width of the body-fitted grids so that any vortices generated by microjets are well-resolved as they travel downstream. These 'near-body' grids are embedded within a set of airfoil-local off-body grids of similar size. Successively larger graded Cartesian box far-field grids are then grown outward until the far-field limits were at least 10,000 chord-lengths from the wing-flap system; a distance deemed necessary by Hosseini et al.[25] due to the research of Destarac,[37] who showed that for lift coefficients greater than one, linearized small-disturbance theory is relevant and perturbation velocities can significantly affect the drag coefficient if far-field boundaries are close to an airfoil.

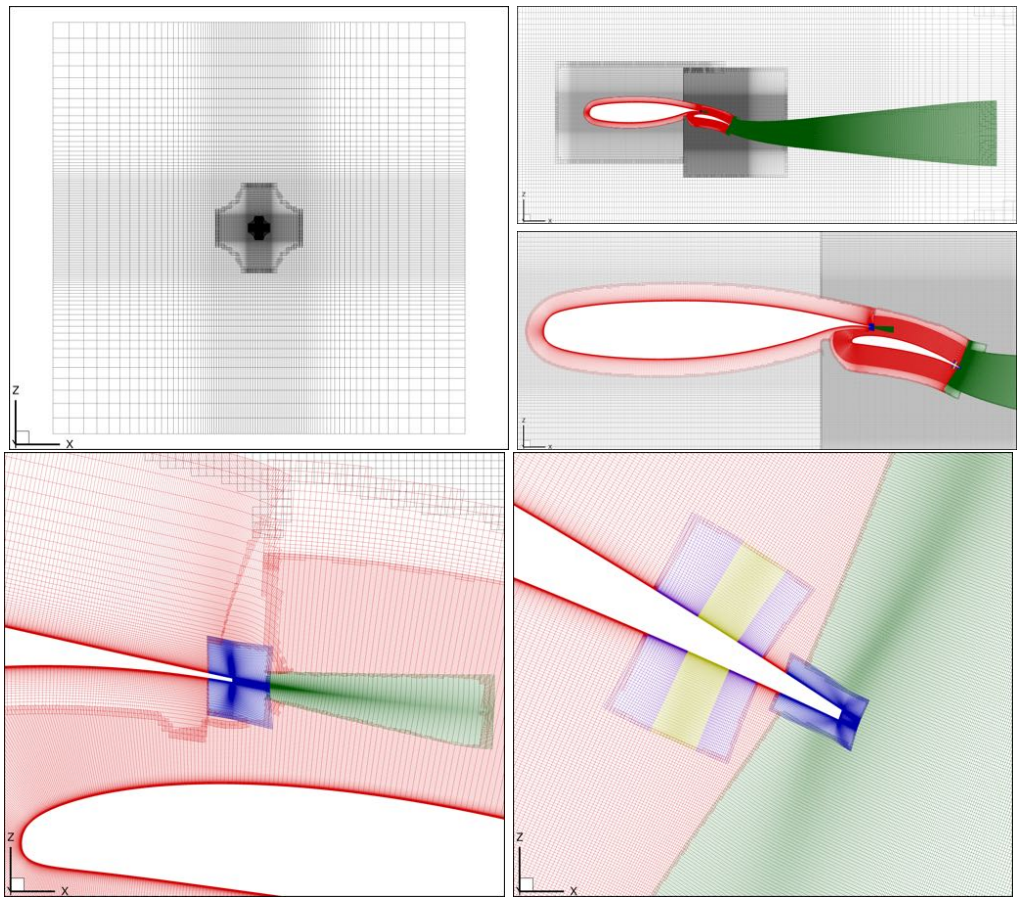

Figure 4. Topology of the overset grid system for the NLR7301 multi-element airfoil. Off-body grids connecting the wing-flap to the far-field are colored black. Body-fitted grids on the wing and flap are shown in red. H-topology grids body-fitted to the trailing edges of the wing and flap are colored blue. Wake grids for the wing and flap are colored green. Microjet grids built on the flap are colored yellow, and the interfaces between them and the wing-flap grids are purple.

Grids representing microjet inflow BCs can be automatically built on the pressure and/or suction side of the flap as needed using the method described at the end of Section III in Figure 3 to cut the side of the flap on which the jet is constructed. The inner portion of the cut becomes the jet inlet and is refined (shown as yellow in the lower right of Figure 4). This jet inlet grid is then graded into the body-fitted flap grid by a connection grid on either side (shown as purple in Figure 4). In the grid system shown in Figure 4, both a pressure and suction side jet were constructed with $l_{jet} = 95\%|\vec{c}|$ and $w_{jet} = 0.5\%c_\infty$. The jets can be modeled as either viscous wall or inflow BCs depending on the case.

While the NLR7301 cases run in this work are 2D, the LAVA solver requires at least three nodes in the symmetry direction, and so the 'width' of the jets in the best practice grid are all $2.0[m]$ centered around $y = 0.0[m]$. All grids were built with a stretching ratio limit of 1.2, regardless of whether they were built on the surface or grown hyperbolically. The first cell height of all body-fitted grids was $2.5 \times 10^{-6}[m]$. There were 27 body-fitted and wake grids required for the wing and flap, 9 off-body and far-field grids, and three grids for each jet, bringing the total grid system to 36 grids consisting of 0.233 million grid nodes with no orphan nodes after they were connected and optimized. Note that this grid size, as with all 2D grids reported

in this work, is for a single 2D plane of the grid, and is thus the total grid size divided by three.

IV.B. Solution Best Practices for Simulating the NLR7301

A second-order accurate conservative finite-difference scheme was chosen to discretize the steady-state RANS equations when simulating the NLR7301 multi-element airfoil. The convective fluxes are evaluated using a modified Roe scheme with third-order upwind-biased reconstruction and utilize the Koren limiter.[38,39] The viscous fluxes are discretized using a conservative mid-point and node-centered difference scheme. For unsteady analysis, the physical time is discretized using an implicit second-order backward difference formula (BFD2). The turbulence model selected for RANS closure is the one-equation Spalart-Allmaras (SA) with negative turbulence variable provisions, rotation and curvature correction (RC) and the quadratic constitutive relation (QCR2000):[40–42] SA-RC-QCR2000. All cases were run using the reference conditions shown in Table 1, in which the reference length l_∞ is the same as the reference wing chord c_∞. At these conditions, the Reynolds and Mach numbers are $Re = 2.51$ million per c_∞ and $M = 0.185$.

Table 1. Reference Conditions for the NLR7301

$p_\infty[Pa]$	$U_\infty[\frac{m}{s}]$	$T_\infty[K°]$	$AOA[°]$	$l_\infty, c_\infty[m]$	$A_\infty[m^2]$
59014.8	62.9559	288.167	6.0	1.0	2.0

Hosseini et al.[22,23,25] showed that time-accurate simulations were required to properly capture the vortex shedding which occurs when microjets are introduced into the NLR7301 system. The required unsteady RANS (URANS) parameters include the physical time step dt for the implicit second-order backward-differencing employed, the number of time steps N required to reach the prescribed physical simulation time t, and a number of sub-iterations (N_{sub}) for which the discretized equations where marched in pseudo-time each time step. The physical time step dt was calculated based on the inverse of the frequency f of the microjet calculated using Equation 5a. This equation is based on the relation between the Strouhal number St of a round object and jet's strength U_{jet} and stream-wise width h_{jet}. For cases without an active jet, f is calculated such that it would take 100 steps for a particle to travel the chord of the wing using free-stream velocity.

Initial URANS simulations made it clear that the unsteady simulations should be cold-started to natrually develop transient flow around the airfoils, and that the fidelity of dt required to capture microjet-induced vortical flow was prohibitively expensive based on the required physical time t needed to develop reported aerodynamic coefficients with a running-average standard deviation within a count for the last 1000 time-steps. Thus, each case was run as a series of consecutive URANS simulations which restarted from the previous with a reduced time step. dt was calculated based on a single pass of f, then decreased based on a factor of four of the current simulation level i as shown in Equation 5b. Here, J are the number of jets within the simulation, across which the smallest frequency determines dt. The number of time steps N required for a given simulation level is calculated based on the physical time for the number of f passes of that level, then bounded based on limits set on the total simulation time as shown in Equation 5c. The chosen best-practice values for the constants in Equations 5a to 5c are shown in Table 2, with the chosen sub-iteration count achieving 4.5 orders of residual reduction each time step.

$$f_{jet} = \frac{StU_{jet}}{h_{jet}} \tag{5a}$$

$$dt_i = \frac{1}{\min\limits_{jet \in J}(f_{jet})4^i} \tag{5b}$$

$$N_i = max\left(\frac{t_{min} \leq t_i \leq t_{max}}{dt_i}\ ,\ N_{min}\right) \tag{5c}$$

Table 2. URANS Time Metric Calculation Values

St	$h_{jet}[m]$	i	$t_{min}[s]$	$t_{max}[s]$	N_{min}	N_{sub}
0.2	$0.5\%c_\infty$	[1,4]	0.1	1.5	4000	5

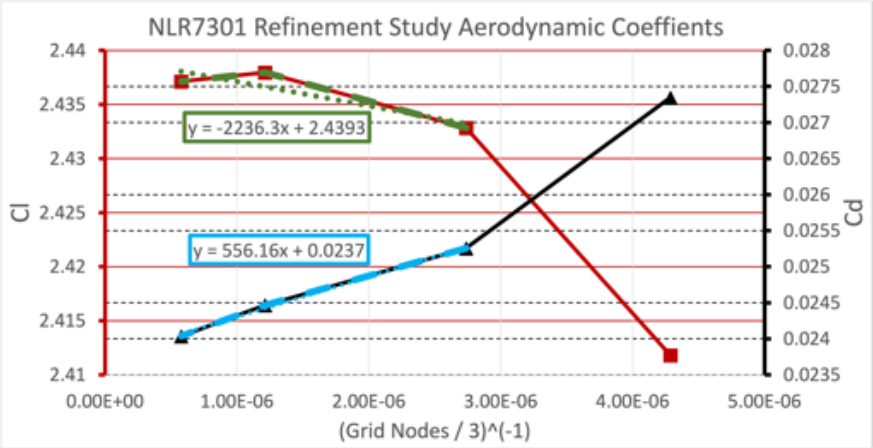

Figure 5. Aerodynamic coefficients of the various refinement study grid levels. Lift coefficient C_l is shown in red, with a Richardson extrapolation linear trend of its finer three grid levels shown in green. Lift coefficient C_d is shown in black, with Richardson extrapolation linear trend of its finer three grid levels shown in blue.

IV.C. NLR7301 Refinement Study

A refinement study was performed for the base grid system constructed using the best-practices described in Section IV.A in order to assess its discretization-related error. This base grid is refined by successively reducing the stretching ratio limit of the surface and volume grids by a fixed factor and then using the corresponding refinement factor to increase grid resolution in all curvilinear directions. The first cell height chosen for the base grid was ensured to have a $y^+ \leq 1$ everywhere as is required by the chosen turbulence model and was kept fixed during refinement. The stretching ratios chosen for the refinement study and the corresponding number of nodes in each grid are shown in Table 3.

The lift and drag coefficients of all grid levels are plotted in Figure 5. In order to perform a Richardson extrapolation on the finer three refinement levels, the data is plotted as a function of h^p, where h is the number of nodes in the dimensions of interest (here, a single 2D sheet of nodes) and p is the observed order of accuracy. p is chosen as the dimensions of interest times $-\frac{1}{2}$. The intercept of the Richardson extrapolations define the theoretically-continuous grid values of the coefficients, and show that on a theoretically infinite grid, the LAVA best practices would yield a C_l of 2.4393 and a C_d of 0.0237.

Coefficient of pressure is plotted on the NLR7301 wing and flap surface in Figure 6. Significant differences can be seen between the base refinement level and its finer counterparts. These differences are particularly noticeable at the wing suction peak and flap suction side near the wing trailing edge, speaking to under-resolution in those areas at the base level. Refinement level 1.913 with a stretching ratio limit of 1.1 is taken as best practice as it is in the middle of the linear trend and sees little change in C_p to its neighboring solutions. This grid level is the one depicted in Figure 4 of Section IV.A for brevity, as the grid topology between levels does not change.

Table 3. NLR7301 Refinement Study Grids

Refinement Factor	Stretching Ratio Limit	Grid Size [million nodes]
1.000	1.200	0.233
1.305	1.150	0.365
1.913	1.100	0.825
3.085	1.075	1.733

IV.D. NLR7301 Jets-Off Experimental Comparison Study

The aerodynamic coefficients of the grid refinement study's best-practice level solution are compared to experimental values[27] and OVERFLOW CFD solutions obtained using published best practices[25] in Table 4. OVERFLOW solutions were run using a central differencing scheme and both the fully-turbulent shear stress transport model (SST),[43] and SA-RC-QCR2000 turbulence model described in Section IV.B. The SST

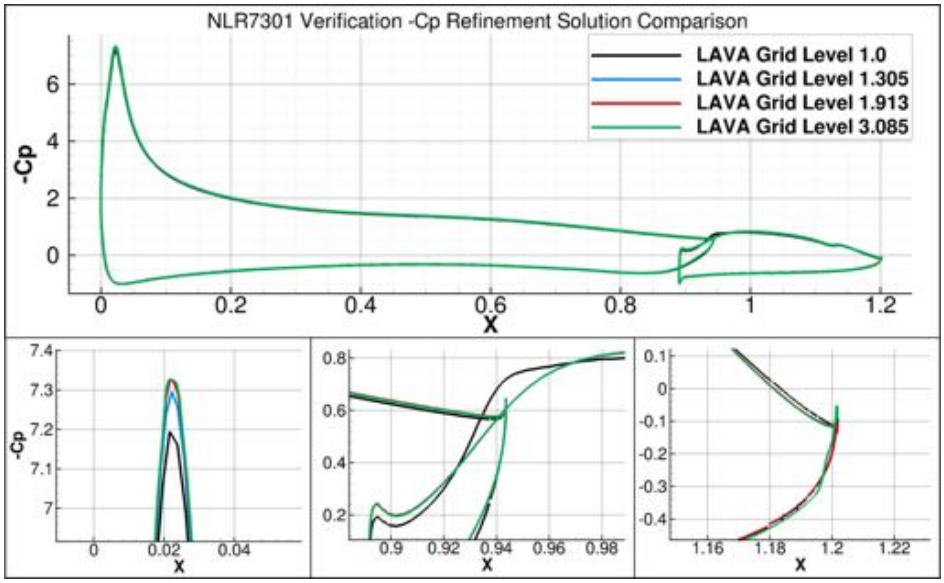

Figure 6. Coefficient of pressure C_p comparison on the surface of the NLR7301 between the four levels of the refinement study. (*Top*): the entire wing-flap geometry. (*Bottom Left*): closeup of the suction peak on the wing. (*Bottom Center*): closeup of the wing trailing edge / flap leading edge. (*Bottom Right*): closeup of the flap trailing edge. x has been normalized by c_∞.

OVERFLOW solution under-predicts experimental value for C_l, while both the LAVA and OVERFLOW SA-RC-QCR2000 solutions over-predict it by a similar amount. All simulations over-predict C_d, with the SA-RC-QCR2000 OVERFLOW solution doing so the least. The experimental accuracy for the experimental C_l and C_d data was reported to be 0.4% and 2.0%, respectively.[27] Figure 7 shows a comparison of coefficient of pressure C_p between experimental, OVERFLOW SST and LAVA SA-RC-QCR2000 best practice CFD solutions. The accuracy for the experimental C_p data was reported to be 0.5%.[27] Both the OVERFLOW and presented LAVA solutions are close to experimental C_p data. Contours of Mach for both CFD solutions are shown in Figure 8, with a slightly faster expansion bubble above and past the flap of the LAVA solution.

Table 4. NLR7301 Refinement Study Grids

	Experimental	OVERFLOW with SST	OVERFLOW with SA-RC-QCR2000	LAVA
C_l	2.42000	2.40800	2.43800	2.43795
C_d	0.02290	0.02499	0.02320	0.02446

IV.E. NLR7301 Code-to-Code Normal-Blowing Comparison Study

Having validated the best practices for simulating the NLR7301 geometry with the LAVA solver, the pressure-side microjet was then turned on and a code-to-code comparison against OVERFLOW data was performed using the wall-normal incompressible jet BC described in Section 9. For this study, the jets of the OVERFLOW grid system were defined with the same flap location and width as described in Section IV.A, and the OVERFLOW solutions used the same turbulence model as the LAVA solver. Figure 9 shows a graphical comparison between the microjet-induced lift increase ΔC_l of the two codes for a range of $C_{\mu,jet}$ values corresponding to $\frac{U_{jet}}{U_\infty} \in [0, 2]$ in increments of 0.2. These ΔC_l curves are fit with with a $K\sqrt{C_{\mu,jet}}$ relation as suggested by Malavard et al.[11] by solving for a K which minimizes the squared error of the fit. The trends are shown to be similar, and find Ks within 0.3% of each other.

V. NLR7301 Compressible Angled Microjet Studies

After the grid construction, solution strategy, and verification and code-to-code comparisons performed in Sections IV.A-IV.E, a series of studies were performed in which the compressible, angled jet BC described in Section III was conditionally imposed on jets constructed on the pressure and/or suction sides of the

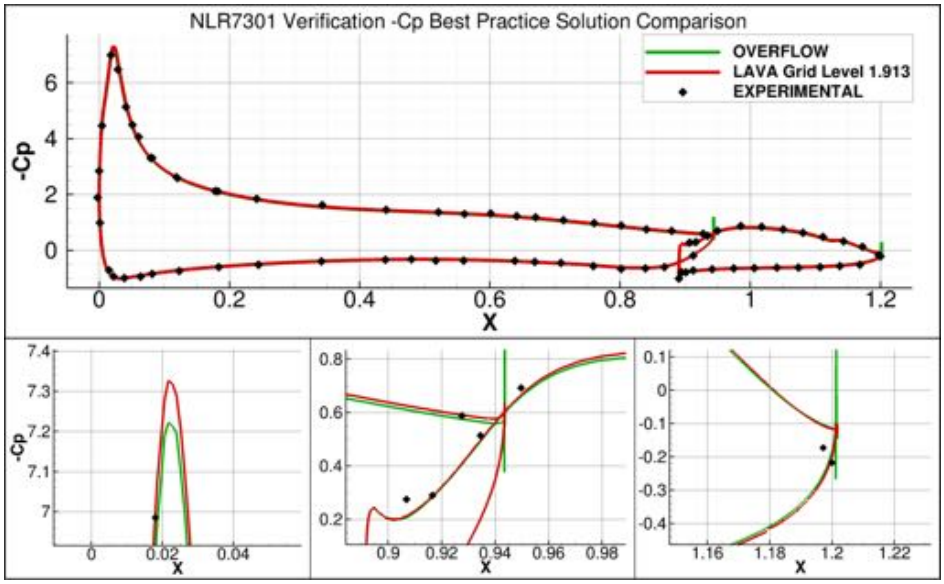

Figure 7. Coefficient of pressure C_p comparison on the surface of the NLR7301 between experimental data and the best practice CFD solutions of OVERFLOW[25] and LAVA. (*Top*): the entire wing-flap geometry. (*Bottom Left*): closeup of the suction peak on the wing. (*Bottom Center*): closeup of the wing trailing edge / flap leading edge. (*Bottom Right*): closeup of the flap trailing edge. x has been normalized by c_∞.

NLR7301 flap as described at the end of Section IV.A. All angle sweeps are performed in increments of 10° from $30 \leq \theta_{jet} \leq 150$. For the denotation of jet angle described in Section III, this corresponds to 30° off of the upstream flap surface to 30° off of the downstream flap surface. For comparability with previously published results, all fixed mass flow rates defined for angle sweeps in this section were calculated from jet parameters that would be used for a normal-blowing incompressible jet BC.

As discussed in Section III, the incompressible angled jet BC can have its parameters calculated in several ways, and the effect of this is explored in Section V.A. The interrelation of jet angle and jet strength for a pressure-side microjet will then be explored in Section V.B, and analyzed as a tool to determine under what circumstances assumption of 'normal-blowing' is valid. Section V.C adds some extra, 'off-nominal' (i.e. infeasibly stronger from a systems perspective) jet strengths to the case matrix run in Section V.B in an effort to explore potential unforeseen impacts to jet aerodynamics caused by certain microjet configurations. Finally, a trade-off study is preformed in Section V.D which compares the effect and interaction of pressure-side normal-blowing microjets and suction-side tangent-blowing microjets on the NLR7301 wing-flap's aerodynamic performance. It should be emphasized that all trends presented are specifically for the NLR7301 flap deflection defined in Section IV.A and the reference conditions described in Section IV.B: for other conditions and geometries conclusions should be drawn from re-computed studies.

V.A. Effect of Jet Parameter Calculation Method

It was noted in Section III that the compressible angled jet needed two of three parameters to be defined: momentum coefficient ($C_{\mu,jet}$), velocity magnitude (U_{jet}), and a mass parameter (density ρ_{jet} or mass flow rate $\dot{m}_{jet}$). If density is chosen, Equation 1 must be used, while if mass flow rate is chosen, Equation 4a must be used instead. It is clear that for two fixed input jet parameters, the third, dependant parameter will be different based on the chosen method. Figure 10 shows an example of this for a θ sweep at a fixed $C_{\mu,jet}$ value of 0.01 and fixed mass parameter from which U_{jet} is calculated. First, ρ_{jet} is held fixed at a 1:1 ratio with the reference density ρ_∞, and the calculated U_{jet} and $\dot{m}_{jet}$ (via Equation 4b) ratios to their reference values are shown to have parabolic profiles. Then, $\dot{m}_{jet}$ is held fixed at the value used for a wall-normal incompressible jet, and the calculated U_{jet} and ρ_{jet} ratios to their reference values are shown to have constant and parabolic profiles, respectively.

This means that while the momentum coming out of two jets may be the same, the velocity and temperature used to define it can be quite different (due to Equation 3). To see if this had an effect on the NLR7301 system, an angle sweep was performed at a $C_{\mu,jet}$ of 0.01 using jet parameters from both calculation methods. Figure 11 shows a comparison of the aerodynamic coefficients C_l and C_d for the two sweeps,

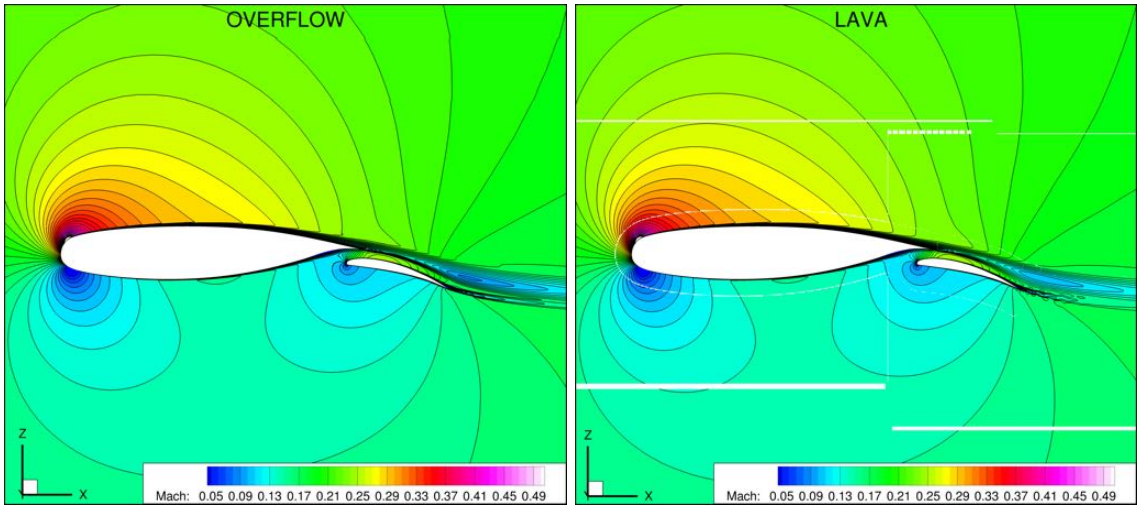

Figure 8. Contours of Mach number for the NLR7301 best practice OVERFLOW SST (*Left*) and presented LAVA SA-RC-QCR2000 (*Right*) CFD solutions. Note that all nodes associated with overset boundary stencils are blanked, creating gaps in the visual solution if two overset boundaries are close to each other.

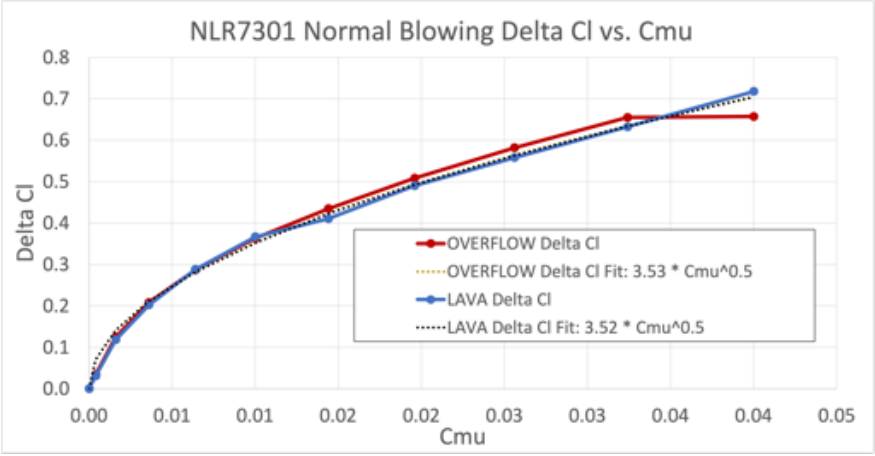

Figure 9. Comparison of the change in lift ΔC_l between the OVERFLOW and LAVA solvers induced by press-side normal-blowing microjets over a range of $C_{\mu,jet}$ values corresponding to $U_{jet} \in [0, 2]$ in increments of 0.2. These trends are fit by a $K\sqrt{C_{\mu,jet}}$ relation, with K being 3.52 for LAVA's trend and 3.53 for OVERFLOW's.

and finds that the differences are minimal: the major influencer on the NLR7301 system is the amount of momentum introduced by the jet. Because of this, mass flow rate is chosen to be the mass parameter for all remaining angle sweeps, as it is a more intuitive engineering parameter.

V.B. Interdependence of Pressure-Side Jet $C_{\mu,jet}$ and θ_{jet}, and their Effect on the Assumption of Normal-Blowing

A case matrix was run examine the interdependence of jet angle and strength for the NLR7301 system given the jet parameters defined in Table 5 for a total of 143 cases. This set of $C_{\mu,jet}$ was chosen to emulate the values chosen in previous works regarding incompressible normal-blowing pressure-side microjets on the NLR7301 flap[22–25,44] corresponding to $\frac{U_{jet}}{U_\infty} \in [0.2, 2]$ in increments of 0.2, with the caveat that the compressible angled jets utilized in this study will result in slightly different velocity ratios for a given $C_{mu,jet}$. These values also represent reasonable jet strengths from a systems engineering perspective. The analysis of trends gleaned from this case matrix will not include fitting them with defined mathematical trends such as $\Delta C_l = K\sqrt{C_{\mu,jet}}$, instead focusing on the variation between trends as $C_{mu,jet}$ and θ_{jet} change.

Before a full analysis of the studies cases is presented, it is helpful to understand the relative importance of the lift and drag components. Normally an aerofoil has only pressure and viscous contributions to lift and drag (C_{lp}, C_{lv}, C_{dp}, C_{dv}), however a jet firing from its surface adds a momentum contribution as well

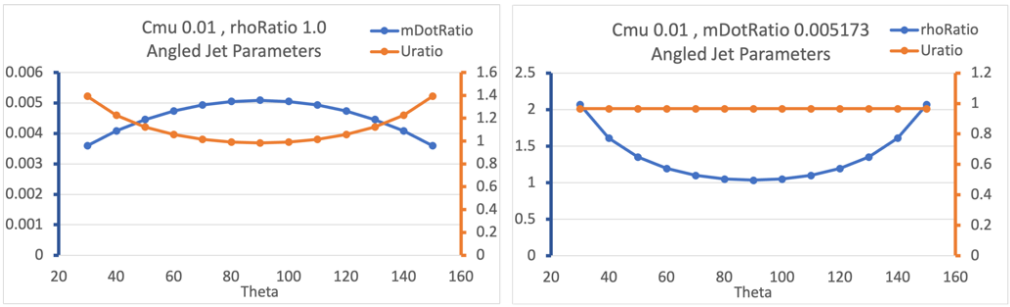

Figure 10. Compressible angled jet parameters calculated for a fixed $C_{\mu,jet}$ of 0.01, first by keeping ρ_{jet} fixed and using Equation 1 (*Left*), and then by keeping $\dot{m}_{jet}$ fixed and using Equation 4a (*Right*). The dependant mass parameter, calculated from the fixed input mass parameter, is also plotted. Differences in the linking of jet parameters between the two equations leads to different jet velocities and temperatures.

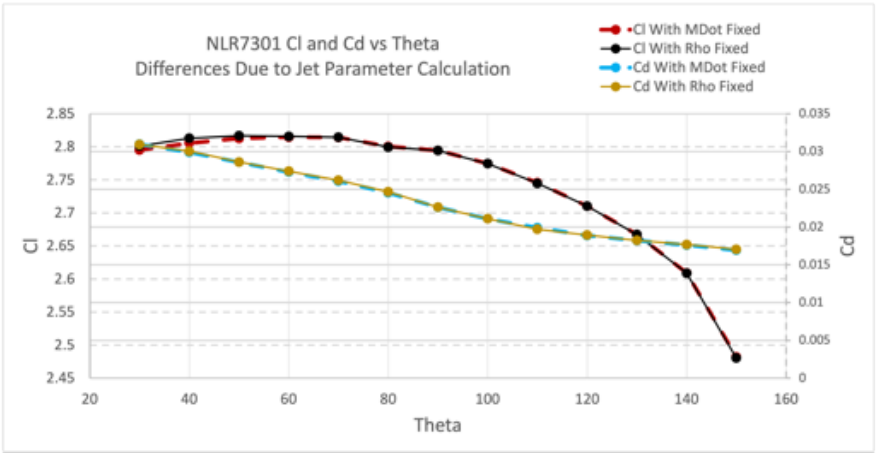

Figure 11. Lift C_l and drag C_d coefficients for two angle sweeps of a jet with $C_{\mu,jet} = 0.01$; one calculated with $\dot{m}_{jet}$ fixed, and the other calculated with $\dot{m}_{jet}$ fixed. Differences are found to be negligible.

Table 5. NLR7301 $C_{\mu,jet}$ vs. θ_{jet} Study Jet Parameters

$C_{\mu,jet}$	0.0004	0.0016	0.0036	0.006	0.01	0.0144
	0.02	0.0256	0.03	0.0324	0.04	
$\frac{\dot{m}_{jet}}{\dot{m}_{\infty}}$	0.001035	0.002069	0.003104	0.004007	0.005173	0.006207
	0.007315	0.008276	0.008960	0.009311	0.010346	

(C_{lm}, C_{dm}) and all three must be accounted for in the total lift and drag. Figure 12 shows three sets of lift and drag components for a few exemplary jet strengths over a range of θ_{jet}. The dominant contribution to lift is C_{lp}, with C_{lv} being four orders and C_{lm} being two orders of magnitude smaller. C_{lv} sees a similar trend-dependence on θ_{jet} as C_{lp}, while C_{lm} varies according to Equation 1. All three components of drag are of a similar magnitude, with C_{dv} being an fairly insensitive to either jet strength or angle and C_{dm} again varying according to Equation 1. It should be noted that C_{lm} and C_{dm} are first analytically calculated using Equation 1 and then transformed by angle of attack (AOA), with the transformation terms becoming zero for C_l at $\theta_{jet} = 30°$ and C_d at $\theta_{jet} = 120°$ when the AOA is 6°.

One focus of this study is to assess how well the assumption of 'normal-blowing' jets holds when θ_{jet} is varied. This is important because although the effects of modeled normal-blowing are promising, flow exiting an actual plenum will have a non-normal effective exit angle influenced by entrainment of free-stream flow within the plenum. Figure 13 shows trends in lift and drag for a range of $C_{\mu,jet}$. Each trend pertains to a specific θ_{jet}. The ΔC_l trends on the left of Figure 13 are inversely parabolic in nature. ΔC_l trends for $40° \leq \theta_{jet} \leq 110°$ lie within a reasonable tolerance of $\theta_{jet} = 90°$, while those outside this range differ significantly and can no longer be fit well with a $K\sqrt{C_\mu}$ relation. The ΔC_d trends shown in the center demonstrate that change in drag has a linear trend with a slope highly dependent on jet angle. This is because the momentum contribution of drag $C_{d,m}$ is on the same order as its viscous and pressure components, and

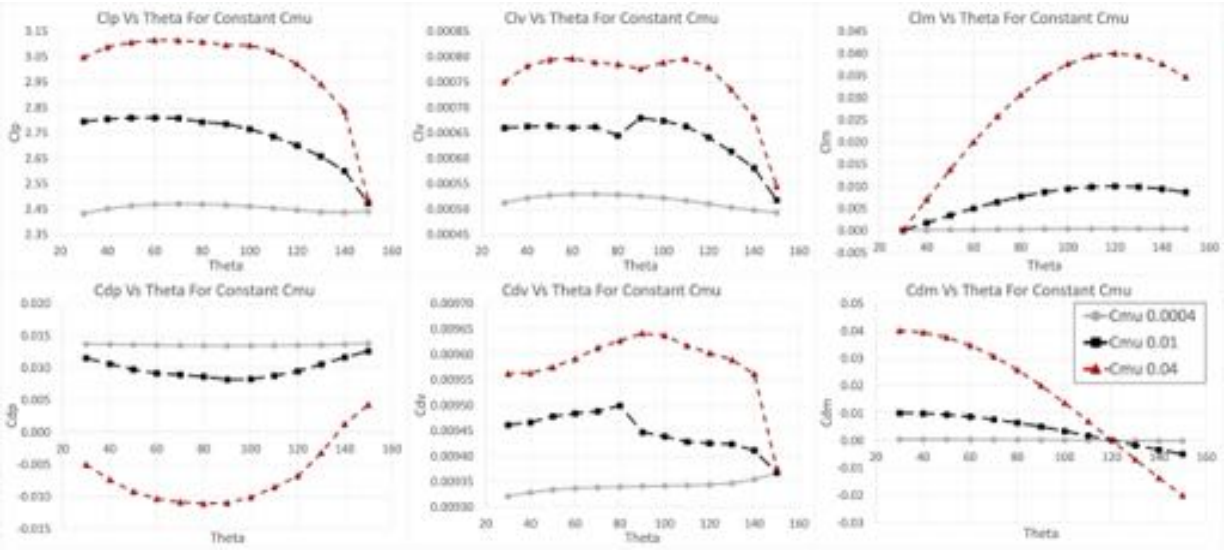

Figure 12. Lift (*Top*) and drag (*Bottom*) components for three constant $C_{\mu,jet}$ trends $\{0.0004, 0.01, 0.04\}$ over a range of jet angles. C_{lp} dominates lift while all components are significant for C_d.

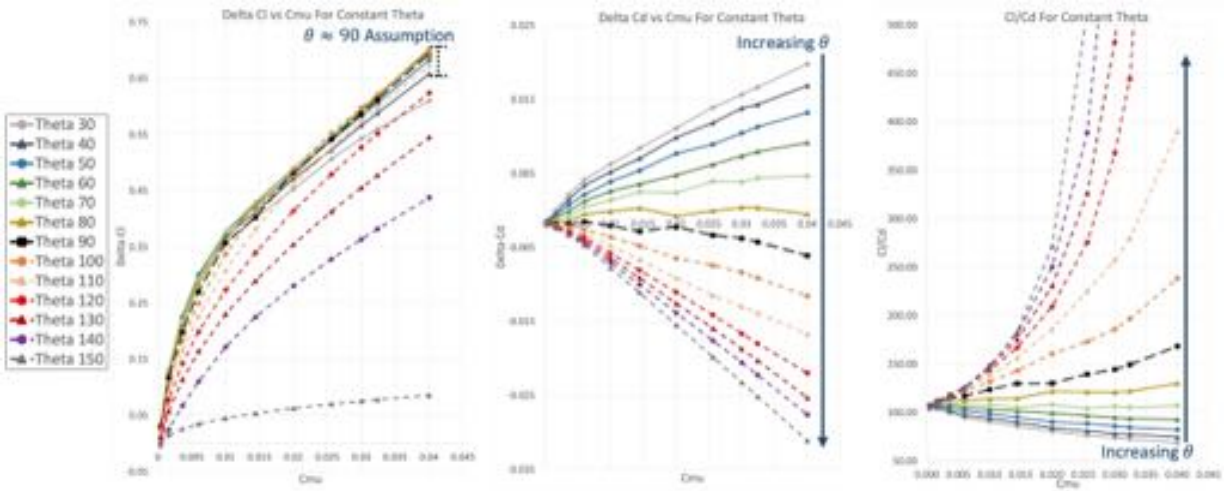

Figure 13. Constant jet angle θ_{jet} trends of (*Left*): ΔC_l, (*Center*): ΔC_d, and (*Right*): $\frac{C_l}{C_d}$ vs. $C_{\mu,jet}$. ΔC_l shows a range of θ_{jet} within which normal-blowing assumptions can be made, but ΔC_d shows strong linear dependence on θ_{jet}.

induces a retro-propulsive or thrusting effect depending on whether the jet is pointing up or downstream. On the right of Figure 13 is the lift to drag ratio, which has an asymptotic trend upwards for downstream theta. This is due to the drag being effectively zero or even negative for stronger pressure-side jets at nearly tangent-blowing since their induced thrust starts to overcome the aerodynamic drag.

Figure 14 shows the same data as Figure 13, rearranged into trends in lift and drag over a range of θ_{jet}. Here, each trend pertains to a specific jet strength $C_{\mu,jet}$. The ΔC_l trends on the left of Figure 13 are parabolic in nature, and have a monotonically increasing zenith with jet strength. The trends collapse to relatively similar lift enhancements at $\theta_{jet} = 150°$ as the effectively tangent-blowing present at this jet angle induces a similar pressure distribution effect regardless of jet strength. This can also be deduced from Figure 14 through the flatness of the $\theta_{jet} = 150°$ ΔC_l curve. For each constant $C_{\mu,jet}$ ΔC_l trend, a range has been placed around $\theta_{jet} = 90°$ within which relative lift changes less than an arbitrarily-defined value (shown by the vertical bars at the end of the ranges). This shows that for a given tolerance, the normal-blowing assumption can be made for a $C_{\mu,jet}$-dependent θ_{jet} interval, with $C_{\mu,jet} = \{0.0036, 0.006\}$ being especially sensitive. The ΔC_d trends shown in the center of Figure 14 have a clear linear regime for $40° \leq \theta_{jet} \leq 120°$ within which the negative slope increases in magnitude with jet strength. This speaks to a relative increase in importance of $C_{d,m}$ relative to its pressure and viscous counterparts. Similarly to Figure 13, the lift-drag ratio seen on the right side of Figure 14 shows an exponential vertical stretching of the sigmoidal trends for

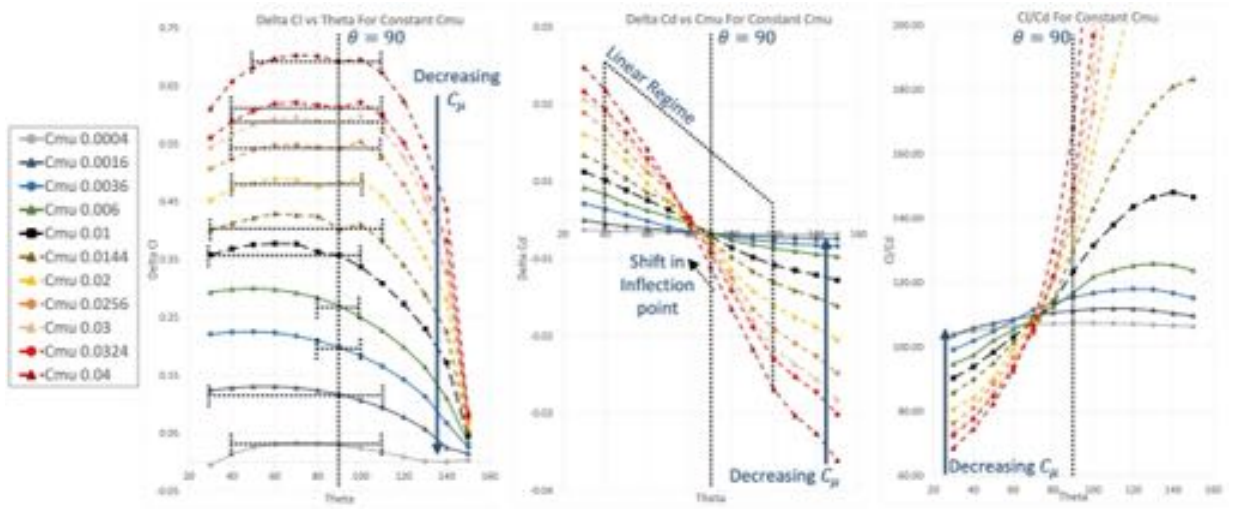

Figure 14. Constant jet strength $C_{\mu,jet}$ trends of (*Left*): ΔC_l, (*Center*): ΔC_d, and (*Right*): $\frac{C_l}{C_d}$ vs. θ_{jet}. ΔC_l shows a $C_{\mu,jet}$-dependent range of θ_{jet} within which normal-blowing assumptions can be made, but ΔC_d shows strong linear dependence on $C_{\mu,jet}$.

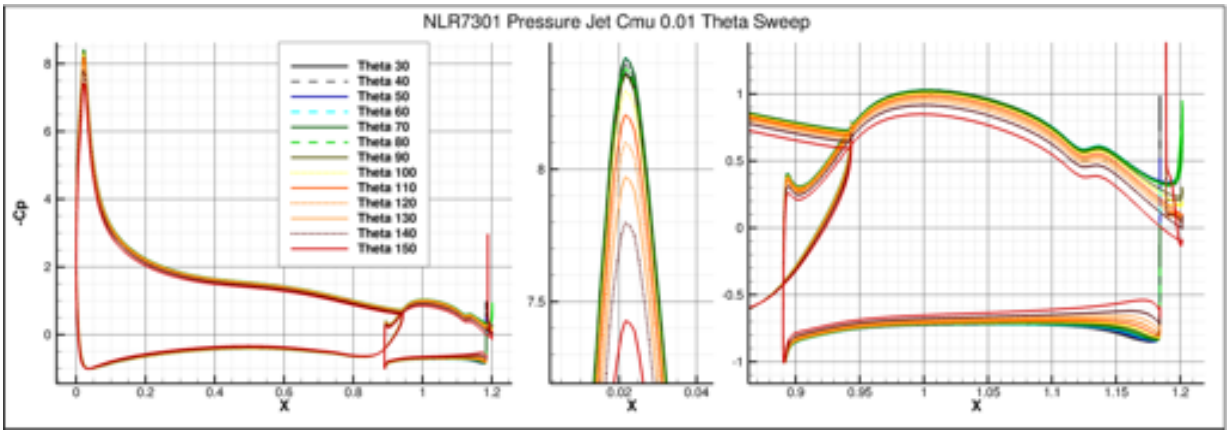

Figure 15. Averaged coefficient of pressure for a constant pressure-side jet strength $C_{\mu,jet}$ of 0.01 over a range of jet angles θ_{jet}. (*Left*): NLR7301 wing-flap system. (*Center*): Suction peak close-up. (*Right*): Flap close-up. C_p profiles correspond logically to the C_l shifts seen in Figure 14. x has been normalized by c_∞.

the higher jet strengths.

The effect of jet strength on the coefficient of pressure (C_p) distribution of the NLR7301 wing-flap system has already been presented in prior research,[22–25,44] but the effect that pressure-side jet angle has on C_p, shown in Figure 15, has yet to be explored. For simplicity, the only a single jet strength ($C_{\mu,jet} = 0.01$) is presented, though its trends are indicative of angle sweeps for all jet strengths in Table 5. Generally, if the jet affects lift to a greater extent, the C_p profile will see a heightening in the suction peak and a shifting right of the pressure valley near the leading edge of the wing. The profiles along the entire top and bottom surfaces of the wing and flap will also shift outward. This clearly demonstrates that a microjet placed near the trailing edge of the flap is able to control the circulation on the main element. The distribution of pressure local to the trailing edge of the flap are driven by the mechanics of vortex formation and the accuracy of flow gradients as vortices pass over the trailing edge corners, and are thus highly specific to both θ_{jet} and $C_{\mu,jet}$. For fixed $C_{\mu,jet}$, increasing θ_{jet} increases the magnitude of C_p shift parabolically. While not shown, For fixed θ_{jet}, the shift in C_p is proportional to jet strength; a result which is consistent with that seen for pressure-side normal-blowing microjets.[25]

V.C. Exploration of Off-Nominal Pressure-side Angled Jet $C_{\mu,jet}$s

The pressure-side microjet strengths of the case matrix presented in Section V.B are representative of mass flows which are conjectured to be nominal (i.e. 'reasonable') from a systems perspective. In this section, similar angle sweeps but with much stronger jet strengths (dubbed 'off-nominal') are presented. This is in

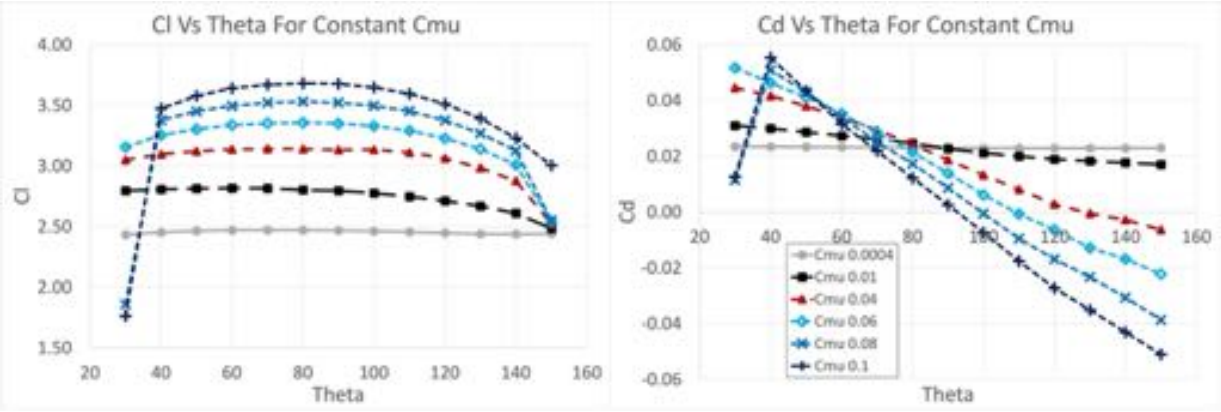

Figure 16. Constant jet angle θ_{jet} trends of (*Left*): C_l and (*Right*): C_d vs. $C_{\mu,jet}$. ΔC_l shows a range of θ_{jet} within which normal-blowing assumptions can be made, but ΔC_d shows strong linear dependence on θ_{jet}.

an effort to explore some of the unexpected effects that can arise from the highly-detailed design variable set possible for microjets, and to emphasize that a robust set of flight conditions should be accounted for during eventual flight testing. The additional cases' jet parameters are found in Table 6. Their lift and drag are plotted along side several jet strength values of the original matrix in Figure 16.

Table 6. NLR7301 Off-Nominal $C_{\mu,jet}$ Study Jet Parameters

$C_{\mu,jet}$	0.06	0.08	0.1
$\frac{\dot{m}_{jet}}{\dot{m}_\infty}$	0.012671	0.014631	0.016358

There are some clear outliers on the trends displayed in aerodynamic and pressure coefficients; specifically for $\theta_{jet} = 30°$ with $C_{\mu,jet} \geq 0.08$ and $\theta = 150°$ with $C_{\mu,jet} \geq 0.10$ (both of which are outside the practical application range of $C_{\mu,jet}$ as noted at the beginning of this section). Looking at the y vorticity plots shown in Figure 17, the prevailing trend with θ_{jet} is that the further upstream the jet faces, the more it pushes against and slows the free-stream flow, de-pressurizing the region behind it and thereby leaving more room for larger vortex formation. As the jet turns to face downstream, the vortices reduce in size until they disappear in what is similar to a tangential-blowing jet. For the two strongest jets pointing upstream at $\theta_{jet} = 30°$, the flow scoops underneath the flap, artificially increasing the width of its seen airfoil. This drastically reduces both lift and drag. When the strongest jet points downstream at $\theta_{jet} = 150°$, it still induces a tangent-blowing effect on the flow, but clearly pushes outward further into the flow than the other jets, which all have roughly the same angle. This causes a different pressure distribution around the NLR7301 wing-flap system when $\theta_{jet} = 150°$, while all other cases collapse to a similar values of C_l, as seen in Figure 16.

Figure 17 shows that while most cases are unsteady when a pressure-side jet is added into the NLR7301 system, some cases are clearly steady. These unsteady regimes were found to be clearly denoted by standard deviation (STD) of C_l, which is plotted in Figure 18. Cases with a C_l STD magnitude above the 'Unsteady Wake' line are highly unsteady and have vortex mixing and formation directly beneath the flap. Cases with a C_l STD magnitude between the 'Steady' and 'Unsteady Wake' lines are strong enough or angled far enough into the flow where wake effects still begin to shear into unsteady vortex patterns, but only downstream of the flap. For most $C_{\mu,jet}$ values, θ_{jet} trends, show that there is an angle beyond which the jet is pointing downstream far enough for its strength to be absorbed by the free-stream, and the flow becomes steady, with its STD falling below the 'Steady' line. The strongest jet, however, sees an intermediate set of angles near $\theta_{jet} = 75°$ for which the jet finds an equilibrium with the free-stream flow it displaces. These cases can also be clearly seen in Figure 17.

V.D. Trade-off of Normal and/or Tangent Blowing Microjets

While tangent-blowing suction side and normal-blowing pressure-side microjets (referred to as 'tangent' and 'normal' microjets in this section hereafter) have been individually studied, little is known about how these two microjet configurations compare to each other individually and when used in tandem. In this section,

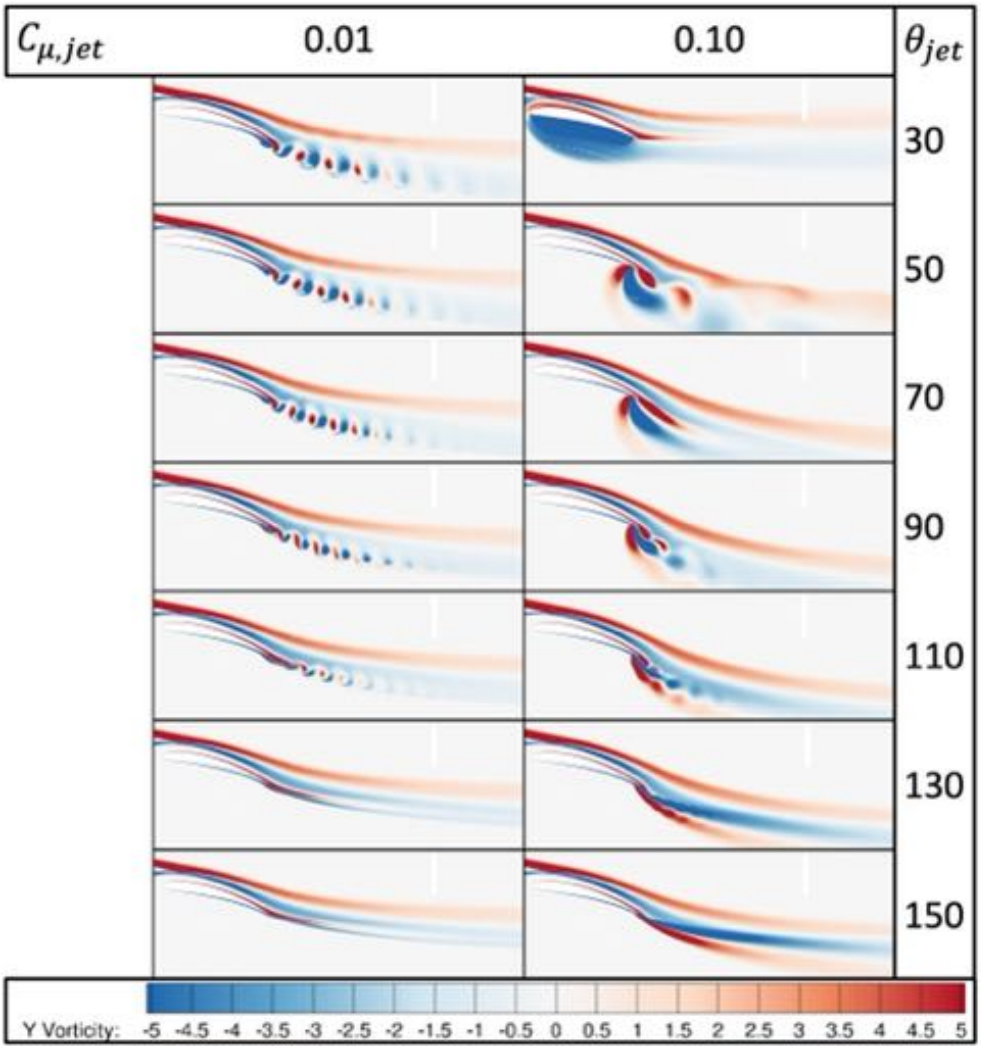

Figure 17. Instantaneous y vorticity of jet angles (*Top*) to(*Bottom*): 30°, 50°, 70°, 90°, 110°, 130°, 150°, for $C_{\mu,jet}$ values of 0.01 (*Left*), and 0.10 (*Right*).

three microjet configurations are presented: tangent, normal and tandem tangent-normal. Both the tangent and normal jets were placed as described in Section IV.A. When turned on, the suction side jet angle, $\theta_{jet,tan}$, is 170°, while the pressure side jet angle, $\theta_{jet,nrm}$, is 90°. Jets were run with one of three conditions - $C_{\mu,jet} = \{0.005, 0.01, 0.02\}$. For a given case, all active jets will have the same jet strength. If we assume that that the NLR7301 system is able to provide a maximum $\frac{\dot{m}_{jet}}{\dot{m}_\infty}$ of roughly 0.0105, then it is possible to have both jets firing with $C_{\mu,jet}$ up to 0.01. The metrics of cases run for this study are shown in Table 7. A trade-off comparison will first be made between the induced lift and drag changes to the NLR7301 wing-flap system for these cases, followed by a visual exploration of how these 2D jets configuration affect the flow of the NLR7301 system to elucidate these findings.

Table 7. NLR7301 Normal-Tangent Trade-off Jet Study Cases

Case ID	0	1	2	3	4	5	6
$\theta_{jet,nrm}$	Off	90	90	Off	Off	90	90
$\theta_{jet,tan}$	Off	Off	Off	170	170	170	170
$C_{\mu,jet}$	0.0	0.01	0.02	0.01	0.02	0.01	0.005
$\frac{\dot{m}_{jet}}{\dot{m}_\infty}$	0.0	0.005173	0.007315	0.005173	0.007315	0.005173	0.003662

The component breakdown and delta shifts of lift and drag of the study cases from case 0 are shown

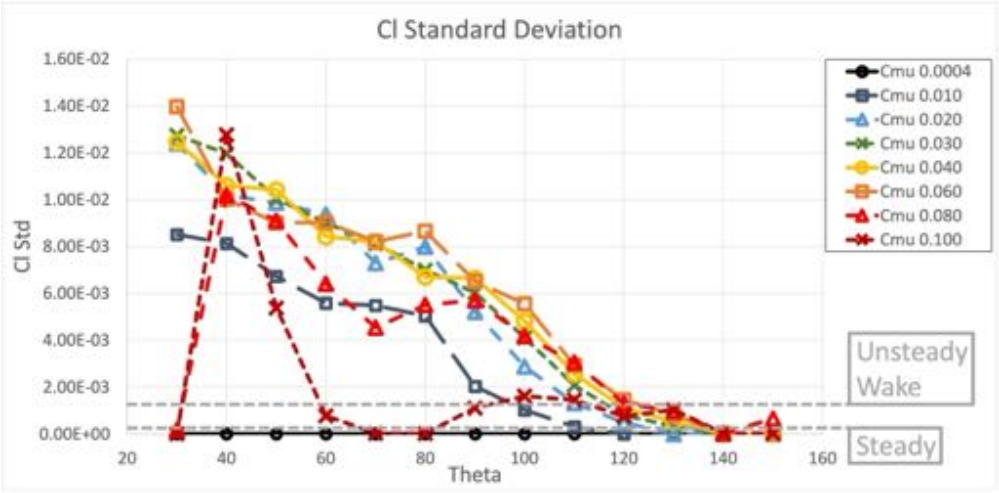

Figure 18. Standard deviations (STDs) of the lift coefficient C_l for various fixed C_μ jet angle sweeps. Flow unsteadiness trends can be ascertained from the STD magnitude. Cases with C_l STDs below the 'Steady' line are completely steady, while cases between it and the 'Unsteady Wake' line have unsteady wakes but no unsteadiness in reported lift or drag. Cases above the 'Unsteady Wake' line are either highly unsteady or unsteady close to the flap such that the reported lift and drag become oscillatory.

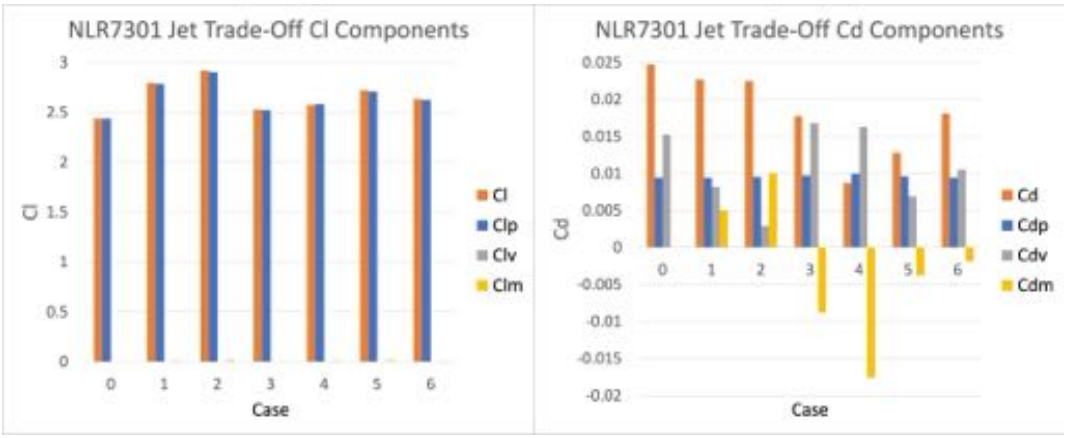

Figure 19. NLR7301 delta lift and drag (ΔC_l and ΔC_d) values for the jet trade-off study. Momentum and viscous components are shown to only have a significant effect on drag.

in Figure 19 and Table 8. As seen in Section V.B previously, the pressure component of C_l dominates its counterparts, while all components of drag have significant contributions. All cases increase lift, with normal-blowing jets increasing it 2-3 times as much as tangent-blowing, and tandem-jet cases falling somewhere in between. This delta C_{lp} trend mimicked in the C_p profiles of the trade-off cases shown in Figure 20, with a greater lift enhancement generally indicated by shifted distance off of the case 0 profile. Similarly to enhancing lift, all cases decrease drag, with the tangent jets decreasing it 3-6 times as much as normal-blowing, and tandem-jet cases again falling somewhere in between. Cases 5 and 6 can be viewed from two perspectives as 'sets'. The first is turning on both tangent and normal jets of a certain strength to see the affect of having both at their full strength, as would be the case for set 1-3-5. The second is have a specific value of $C_{\mu,jet}$ that can be introduced, which can come from either a single tangent or normal jet or split between them when both are on. This would be the case for sets 1-3-6 and 2-4-5. Flow visualization of y vorticity for trade-off cases 0, 1, 2, 4, and 5 are found in Figures 21-25. Case 0 is shown to have a slightly unsteady wake which, as discussed in Section V.B, is small enough to not induce oscillations in lift and drag. Flow from the pressure side of the flap expands into the free air after the trailing edge and rolls into a slight recirculation as it is pulled into the lower pressure region just aft of the flap.

When a normal-blowing jet is placed on the pressure side of the flap as seen for case 1 in Figures 22, a low pressure region is created aft of the flap which draws flow around the trailing edge from the suction side. This flow curls and expands into a vortex which travels down stream and induces a shearing vortex pattern large enough to cause oscillatory loading on the wing-flap system. The resulting change in the pressure field

Table 8. NLR7301 Jet Trade-off Study Lift and Drag Deltas

	ΔC_l	ΔC_{lp}	ΔC_{lv}	ΔC_{lm}	ΔC_d	ΔC_{dp}	ΔC_{dv}	ΔC_{dm}
Case 1	0.356758	0.348192	0.000237	0.008663	-0.002046	-0.007086	-0.000006	0.004995
Case 2	0.482600	0.465022	0.000248	0.017329	-0.002256	-0.012351	0.000103	0.009992
Case 3	0.088716	0.084153	-0.000160	0.004756	-0.006971	0.001525	0.000289	-0.008797
Case 4	0.137056	0.146895	-0.000275	0.009512	-0.016038	0.001026	0.000510	-0.017593
Case 5	0.284201	0.270871	0.000049	0.013419	-0.011909	-0.008318	0.000148	-0.003802
Case 6	0.193949	0.187207	0.000088	0.006710	-0.006606	-0.004732	0.000015	-0.001901

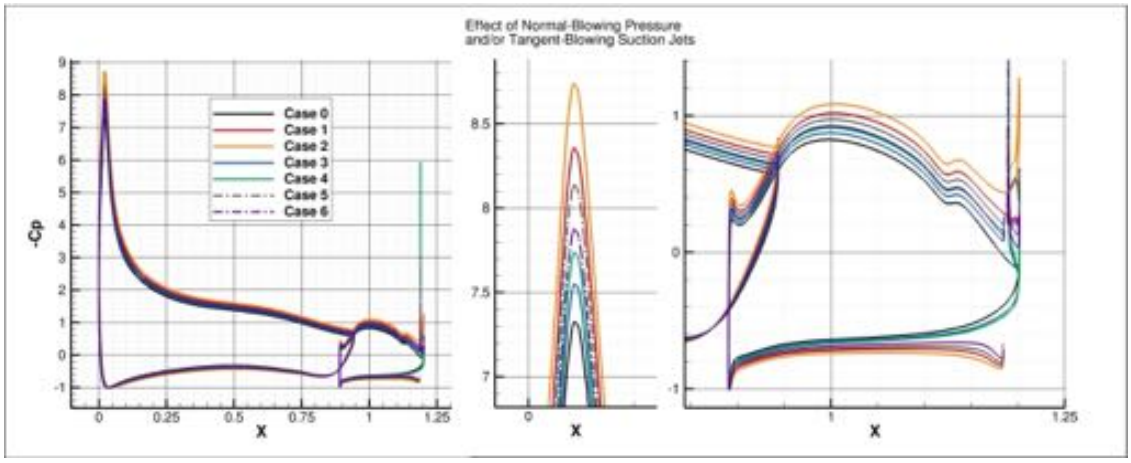

Figure 20. Averaged coefficient of pressure for the normal-tangent NLR7301 microjet trade-off study cases. (*Left*): NLR7301 wing-flap system. (*Center*): Suction peak close-up. (*Right*): Flap close-up. C_p profiles correspond logically to the C_{lp} shifts seen in Figure 19. x has been normalized by c_∞.

effectively increases the camber of the airfoil by shifting the rear stagnation point. The reduction in drag seen for the normal-blowing cases in Figure 19 is due to the reduction in its viscous contribution, C_{dv}, which is altered on the pressure side of the wing-flap system due to the blockage introduced by the normal jet flow. If the strength of this jet is increased, as shown for case 2 in Figure 23, the low pressure region created by the normal-blowing jet is now stronger, and pulls more flow around the trailing edge with greater energy. The result is a larger vortex which breaks into a 'sawtooth' pattern and induces minor sub-oscillations that can be seen within the lift and drag trends. Generally, the sawtooth vortices get larger and spin faster the stronger the jet, and the shearing wake pattern has a lower frequency with larger amplitude vortex pairs due to the counter swirl of the jet wake caught up by the sawtooth vortex as it travels downstream.

If a tangent-blowing jet is turn on as shown for case 4 in Figure 24, the strong shear layer coming off the suction side of the flap induces a small vortex roll-up which fights the flow that would normally expand into the trailing edge region from the pressure side of the flap as seen in case 0 (Figure 21). This stabilizes the wake flow and turns the solution truly steady. The increase in lift seen for cases 3 and 4 in Figure 19 is due to the effective lengthening of the airfoil chord cause by this trailing edge interaction. The significant decrease in drag seen by the tangent jets is due to the thrusting nature of these jets since their momentum overpowers the other drag components. When both normal and tangent jets are turned on, as seen in Figure 25, the tangent jet's flow off the suction side of the trailing edge enhances the energy and size of the vortex that is being pulled over into the low-pressure region aft of the normal jet. When this vortex travels downstream the flow from the normal jet is quickly pulled into its absence, inducing a much higher frequency shearing wake. Depending on how the cases are compared, their set's tandem jet case's lift and drag can be destructive or additive when both jets are firing compared to their single jet cases. For all case sets firing both jets has an additive effect on viscous lift and a destructive effect on viscous drag. For the set 1-3-5, where both jets are firing at their original strength, firing both jets has a destructive effect on pressure lift and drag, but an additive affect on momentum lift and drag. For sets where the tandem firing jets have split the $C_{\mu,jet}$ of the single jets (1-3-6 and 2-4-5), both pressure and momentum lift is destructive while both pressure and momentum drag is additive.

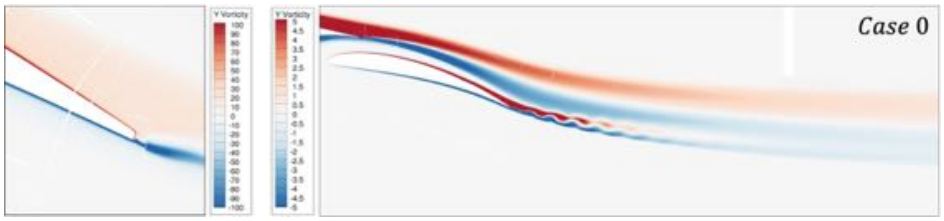

Figure 21. Y vorticity for case 0 of the NLR7301 microjet trade-off study. (*Left*): close up of flap trailing edge. (*Right*): flap wake.

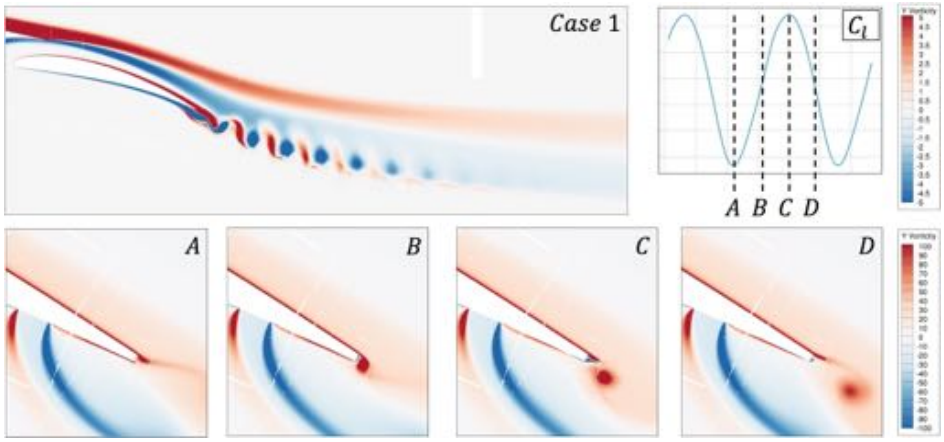

Figure 22. Y vorticity for case 1 of the NLR7301 microjet trade-off study. (*Top Left*): close up of flap trailing edge. (*Top Right*): oscillatory C_l designating flap trailing edge snapshot cycle location. (*Bottom*): close up snapshots of flap trailing edge.

VI. Best Practices for Simulating the CRM-HL with LAVA Curvilinear

The High Lift Common Research Model (CRM-HL) has been the subject of the AIAA High Lift Prediction Workshop (HLPW) since 2011.[45–48] The goal of the HLPW is to assess the current state-of-the-art in high-lift prediction capabilities, as well as collating and analyzing computational results for the CRM-HL. Solutions have been contributed to the workshop using the LAVA solver for HLPW3[29] and HLPW4.[31] The CRM-HL geometry designed for HLPW4 was used in this work to investigate the effects of implementing angled microjets on the inboard flap. As shown in Figure 26, this CRM-HL geometry is a half-span representation of a model that was originally tested within the QinetiQ 5-meter wind tunnel,[28] but is simulated in free air in this work. The model consists of a multi-element wing which includes both inboard and outboard leading edge slats, a stationary main wing element, and inboard and outboard flaps that are deflected to 40° and 37°, respectively (i.e. the nominal deflections).

The CRM-HL case was simulated using the best practice grid and solution metrics determined for LAVA.[31] Scheme and flux solution best practices were the same as those selected in Section IV.B for the NLR7301 solutions. However, the turbulence model selected for RANS closure of the CRM-HL cases is the uncorrected one-equation SA model and the solutions are run using steady RANS, because using them lead to the most consistent solutions between codes in HLPW4. The level 'C' LAVA grid was used for all cases run in this work, which consisted of 223.5 million solution points, a target y^+ of 1.0, and a maximum grid stretching ratio of 1.1. All cases were run using the free-stream reference conditions shown in Table 9. At these conditions, the free-stream Mach and Reynolds numbers are $M = 0.2$ and $Re = 5.49$ million per foot. An angle of attack (AOA) of 7.05 was chosen so that the highly separated flow features seen at higher AOAs of the workshop are not present.

Table 9. Reference Conditions for the CRM-HL

$p_\infty[Pa]$	$U_\infty[\frac{m}{s}]$	$T_\infty[K°]$	$AOA[°]$	$c_\infty(MAC)[m]$	$A_\infty[m^2]$
17143.3	68.2221	289.444	7.05	7.00532	191.845

The baseline solution found using these best practices can be seen in Figure 27. The solution was run for 10000 non-linear iterations, with standard deviations of lift and drag over the last 1000 iterations falling

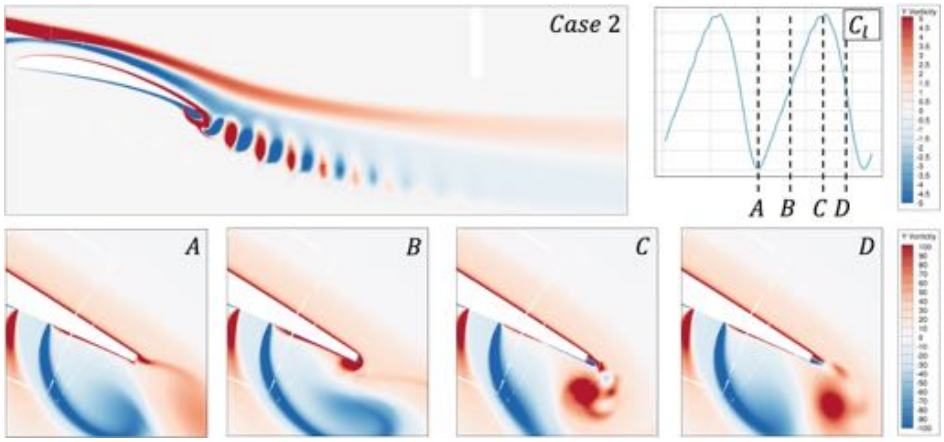

Figure 23. Y vorticity for case 2 of the NLR7301 microjet trade-off study. (*Top Left*): close up of flap trailing edge. (*Top Right*): oscillatory C_l designating flap trailing edge snapshot cycle location. (*Bottom*): close up snapshots of flap trailing edge.

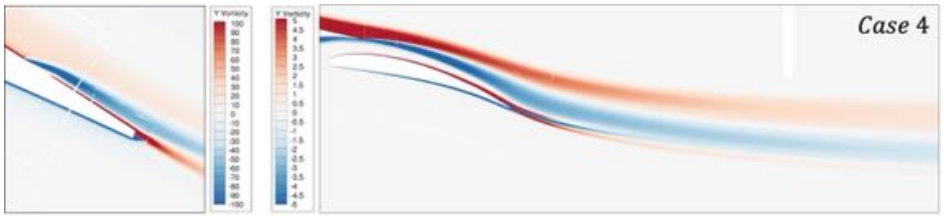

Figure 24. Y vorticity for case 4 of the NLR7301 microjet trade-off study. (*Left*): close up of flap trailing edge. (*Right*): flap wake.

below a drag count, and a residual reduction of 4.5 orders. For the baseline (no-jets) case computed using the best practices described above, the total lift and drag of all components can be found in Table 10. However, to make the CRM-HL case more analogous to the NLR7301 solutions assessed earlier, and because microjets will only be placed on the inboard flap, reported lift and drag for the CRM-HL within the studies that follow will only account for the slat, wing and flaps unless explicitly stated. The reported baseline case's lift and drag components can be found in Table 11. Figure 27 shows a large separation can be seen on the outboard portion of the inboard flap due to the interaction of the nacelle wake and the flap track fairing blockage as flow turns over the flap's trailing edge. Several smaller separations near the trailing edge on the inboard portion of the inboard flap can also be seen. The outboard flap has a large, constant chord-wise separation at 50% of the flap chord starting at around 25% of its span. These separation patterns are consistent with what was reported in HLPW4.[31]

Table 10. CRM-HL Baseline Solution Total Lift and Drag

$C_{l,tot}$	$C_{d,tot}$
1.756515	0.182986

Table 11. CRM-HL Baseline Solution Lift and Drag ∈ Slat+Wing+Flaps

C_l	C_{lp}	C_{lv}	C_d	C_{dp}	C_{dv}
1.475835	1.475603	0.000233	0.143996	0.136618	0.007377

VII. CRM-HL Compressible Angled Microjet Studies

In order to analyze the 2D findings of the NLR7301 studies performed in Sections V.B and V.D for differences that can arise from 3D effects, a pair of studies was performed for the CRM-HL similar to some

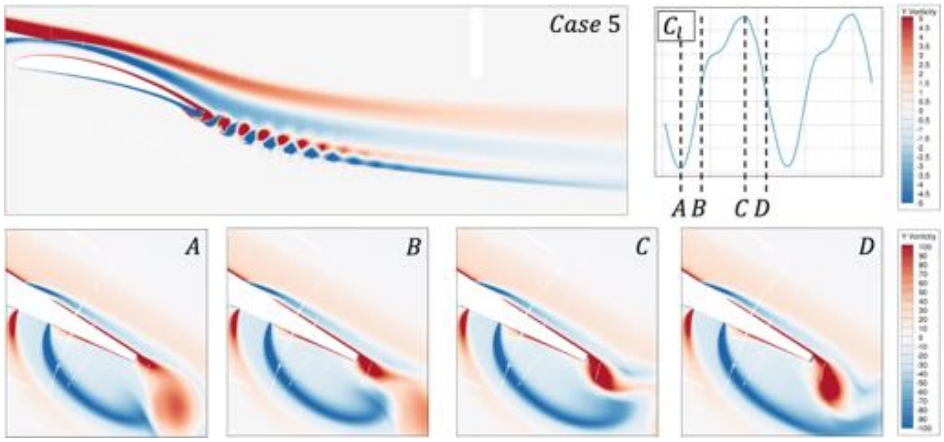

Figure 25. Y vorticity for case 5 of the NLR7301 microjet trade-off study. (*Top Left*): close up of flap trailing edge. (*Top Right*): oscillatory C_l designating flap trailing edge snapshot cycle location. (*Bottom*): close up snapshots of flap trailing edge.

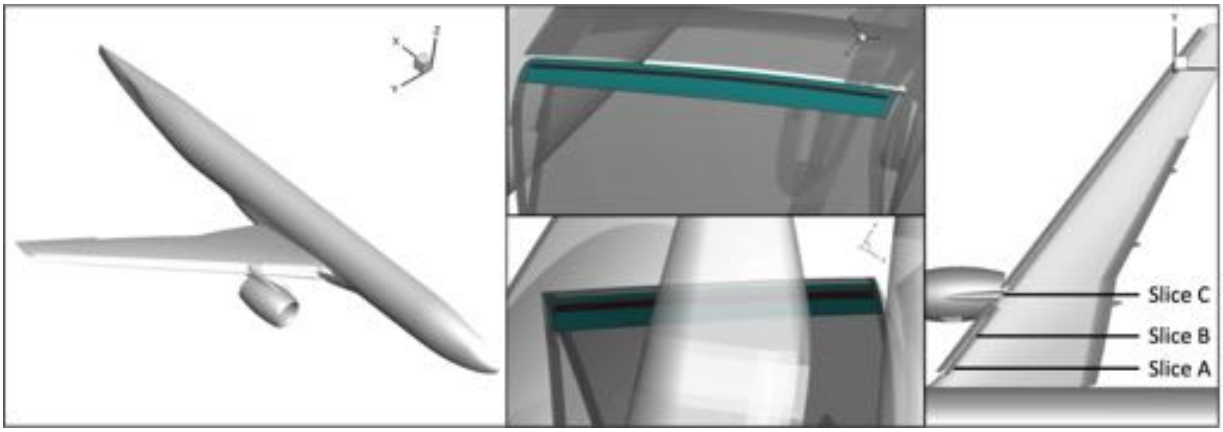

Figure 26. (*Left*): Half-body geometry of the CRM-HL used for HLPW4. (*Center Top*): Placement of microjet grids onto the suction side of the inboard flap. (*Center Bot*): Placement of microjet grids onto the pressure side of the inboard flap. The jet grids themselves are red, while the grids connecting them to the original flap grids via overlap are teal. (*Right*): Slice locations used to extract C_p (see Section VII).

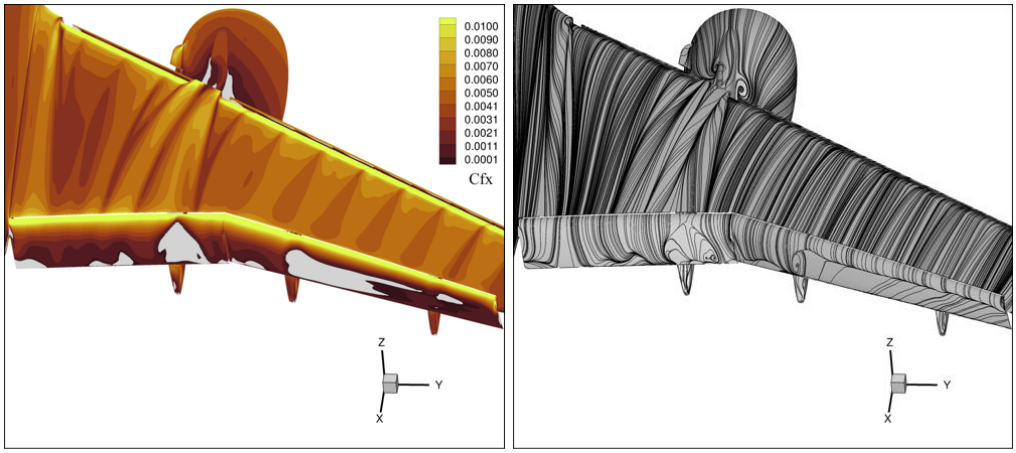

Figure 27. Baseline solution of the CRM-HL found using best practices. (*Left*): surface C_{fx} on the wing with cutoff below zero marking recirculation zones. (*Right*): surface streamlines on wing.

run for the NLR7301. A single microjet was placed on both the pressure and suction sides of the inboard flap. The span-wise length of the jets was chosen to be 95% of the flap span (2.5% offset from the ends of the flap) and the widths of the jets were chosen to be 0.5% of the Mean Aerodynamic Chord (MAC) in order to match Hosseini et al.[30] Jet construction is performed the same way as described for 2D in Section III, but extended to 3D: the chord vector surface of the flap is discretized, and the chord-wise projection of the

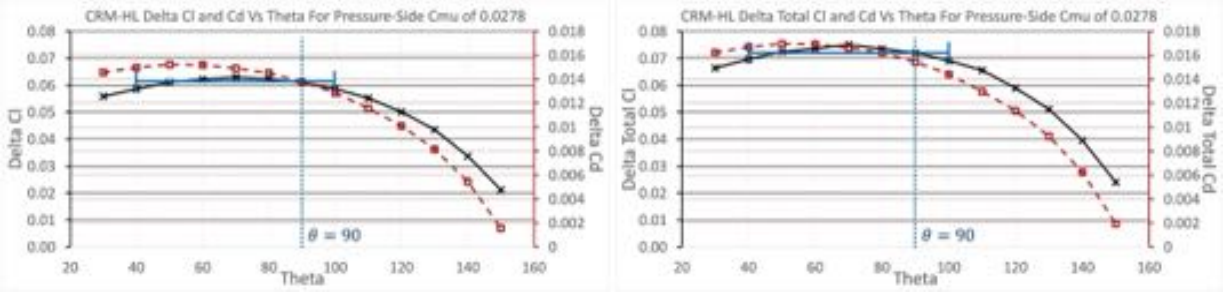

Figure 28. CRM-HL delta lift and drag (ΔC_l and ΔC_d) values for each θ_{jet} in the constant $C_{\mu,jet}$ sweep. (*Left*): lift and drag on the slat+wing+flaps. (*Right*): lift and drag on all CRM-HL components. ΔC_l shows a $C_{\mu,jet}$-dependent range of θ_{jet} within which normal-blowing assumptions can be made.

jet onto the flap surface is performed at each span-wise chord vector of the surface. The projected set of microjet segments is then splined together and connection grids are built to overlap it properly with the flap grids. The jet angle rotation axis' start is defined as half-way between the center of the entire jet surface and the center of the jet surface's starting (inboard) edge. Its end is similarly defined, but with the center of the jet surface's ending (outboard) edge. The average jet normal is rotated around this axis and the jet area is projected onto its plane to find the rotated jet area.

The pressure-side jet's l_{jet} was centered at 95% of the inboard flap chord in order to mimic the best practice normal-blowing location found for the NLR7301. The location of the tangent-blowing suction jet on the NLR7301 was the same as the pressure-side jet because that is where the separation on the flap occurred. For the CRM-HL it makes more sense to place it just upstream of the large separation region seen in Figure 27 as its purpose is to re-energize the boundary layer and mitigate that separation. Thus, it was centered with l_{jet} of 4.75% of the inboard flap chord. These microjets are visualized on the inboard flap surface in Figure 26. It should be underlined that the decided-upon flap chord locations and jet strengths of the tangent and normal-blowing jets within the following studies are simply academic and are not meant to represent optimized or engineered flap microjets. In Section VII.A, only the pressure-side microjet is turned on, and a single jet-angle sweep is performed to see if the delta lift and drag trends corroborate those found for the NLR7301. Next, in Section VII.B, the effect and interaction of pressure-side normal-blowing microjets and suction-side tangent-blowing microjets on the CRM-HL's aerodynamic performance is assessed. For the discussions in these sections, which involve comparison of NLR7301 and CRM-HL results, it is important to remember that the cases are not strictly comparable as they are entirely different geometries and have different flap deflections.

VII.A. Effect of Inboard Flap Pressure-Side Jet angle θ_{jet}

A jet angle sweep was performed using the pressure-side microjet on the CRM-HL's inboard flap. During the sweep, jet strength and mass flow $C_{\mu,jet}$ and $\frac{\dot{m}_{jet}}{\dot{m}_\infty}$ were fixed at 0.00278 and 0.001390 - values determined by assuming 'normal-blowing' for a $\frac{U_{jet}}{U_\infty}$ of 1. Unlike for the 2D NLR7301 case, the momentum components of both lift and drag are quite small relative to their pressure and viscous counterparts. Comparing the $C_{lm} = 0.001628$ and $C_{dm} = 0.002118$ values found for the jet angle sweep's $\theta_{jet} = 90$ case to those in Table 11 concludes that the 3D CRM-HL geometry sees a drastically lower momentum-to-non-momentum drag ratio than the 2D NLR7301 solutions. These momentum values are of the same order seen by Hosseini et al.[30] ΔC_l and ΔC_d throughout the angle sweep are shown in Figure 28. Both the delta lift and drag trends are parabolic in nature: the delta lift curve across θ_{jet} is of a similar format to that seen in the NLR7301 solution matrix shown in Figure 14 but the delta drag curve does not share the same linear trend found for the NLR7301. This is because at its relative magnitude, the momentum drag cannot influence drag trends as it does with the NLR7301. Figure 28 shows delta trends for both the total lift and drag (over the entire CRM-HL) as well as the reported (slat+wing+flaps) lift and drag. The trends display very little difference in shape between them, showing that the main trend variations should appear in the reported slat+wing+flaps lift and drag. Similarly to Figure 14, a range has been placed around $\theta_{jet} = 90°$ within which relative lift changes less than an arbitrarily-defined value (denoted by the vertical bars at the end of the range). This shows that for this chosen tolerance and jet strength, the normal-blowing assumption can be made for $100° < \theta_{jet} < 40°$.

Figure 29 shows C_{fx} and streamlines on the inboard flap's suction-side surface. After the pressure-side

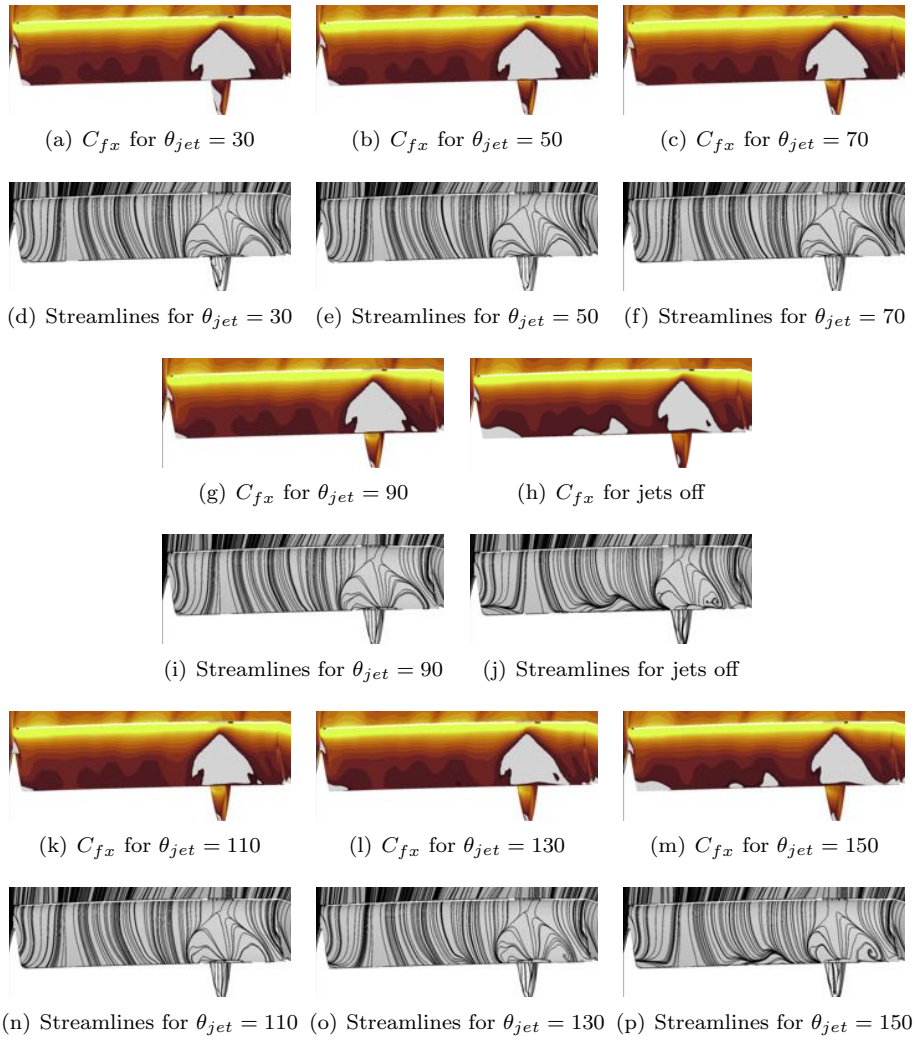

(a) C_{fx} for $\theta_{jet} = 30$ (b) C_{fx} for $\theta_{jet} = 50$ (c) C_{fx} for $\theta_{jet} = 70$

(d) Streamlines for $\theta_{jet} = 30$ (e) Streamlines for $\theta_{jet} = 50$ (f) Streamlines for $\theta_{jet} = 70$

(g) C_{fx} for $\theta_{jet} = 90$ (h) C_{fx} for jets off

(i) Streamlines for $\theta_{jet} = 90$ (j) Streamlines for jets off

(k) C_{fx} for $\theta_{jet} = 110$ (l) C_{fx} for $\theta_{jet} = 130$ (m) C_{fx} for $\theta_{jet} = 150$

(n) Streamlines for $\theta_{jet} = 110$ (o) Streamlines for $\theta_{jet} = 130$ (p) Streamlines for $\theta_{jet} = 150$

Figure 29. CRM-HL inboard flap suction-side surface C_{fx} and streamlines for the fixed pressure-side microjet $C_{\mu,jet}$ sweep of θ_{jet}. C_{fx} has a cutoff below zero marking recirculation zones.

jet is turned on, the Coanda effect it induces causes the flow to re-attach the small inboard separations seen when no jets are on. The large separation above the flap track fairing is largely unaffected because it displaces the jet's flow and pressure field effect. This jet-on separation pattern is quite static for all θ_{jet}s of the sweep, but returns to the jet-off pattern when the jet angle effectively becomes tangent-blowing at $\theta_{jet} = 150°$ since the Coanda effect is no longer being induced. Figure 30 shows slices of C_p taken at locations A, B and C denoted in Figure 26. The large lower profile gap seen in slice C is where the flap track fairing is attached to the wing. The profile trends seen at slices A and B share broad similarities with those seen for the NLR7301 in Figure 15. A shifting of C_p just upstream of the pressure-side jet shows the blockage effect the jet has locally, with profiles moving outward as the jet is angled upstream from $\theta_{jet} = 90°$ and inward as the jet is angled downstream. At slice C, the pressure-side flap C_p profile differs drastically for $\theta_{jet} = 150°$ compared to the other jet angles. On the suction side of the wing and flap at slices A and B, the induced pressure profile reaches a maximum outward displacement at $\theta_{jet} = 60°$, and then moves back inward with $\theta_{jet} > 50°$ being further inward then the $\theta_{jet} = 90°$ profile. Angling the jet downstream strictly moves the suction-side profile inward. The suction side profiles at slice C are fairly insensitive to θ_{jet} as this is in the separation region which is shielded from the jet's effect by the flap track fairing. A strengthening of the suction peak is seen for $\theta_{jet} = 150°$. This in conjunction with its profile deviation on the flap's pressure side indicates that the effectively tangent-blowing jet induces flow to be sucked through the gap between the wing and inboard flap. Thus, for the range of 'normal-blowing-effective' jet angles determined in Figure 28, no unexpected C_p trends are found.

VII.B. Trade-off of Inboard Flap Normal and/or Tangent-Blowing Microjets

Similarly to Section V.D, the following study looks at the trade-offs between three microjet blowing configurations on the inboard flap of the CRM-HL: a single suction-side tangent-blowing jet with angle $\theta_{jet,tan}$, a single pressure-side normal-blowing jet with angle $\theta_{jet,nrm}$, and both jets in tandem. The jet parameters for each case in the study are shown in Table 12. The nominal jet strength of is the same one chosen for the angle sweep study presented in Section VII.A. The individual jet cases 1 and 2 use parameters calculated using this strength, tandem jet case 3 finds its parameters by splitting the nominal $C_{\mu,jet}$ between them, and tandem case 4 uses the parameters of both individual jets unchanged. When turned on, the suction side jet angle, $\theta_{jet,tan}$, is 170°, while the pressure side jet angle, $\theta_{jet,nrm}$, is 90°. The relative effect that these jet configurations have on the CRM-HL's lift and drag will first be explored, followed by an analysis of the flow phenomena which arise through their application.

Table 12. CRM-HL Normal-Tangent Trade-off Jet Study Cases

Case ID	0	1	2	3	4
$\theta_{jet,nrm}$	Off	Off	90	90	90
$\theta_{jet,tan}$	Off	170	Off	170	170
$C_{\mu,jet}$	0.0	0.00278	0.00278	0.00139	0.00278
$\frac{\dot{m}_{jet}}{\dot{m}_\infty}$	0.0	0.001390	0.001390	0.000983	0.001390

A lift and drag component breakdown is shown for the trade-off study cases in Figure 31. As discussed in Section VII.A, the relative contribution of momentum to drag is much less for the 3D CRM-HL than it was for the 2D NLR7301, meaning that because the viscous contributions are more-or-less the same between the cases, changes in reported lift and drag are dictated by the pressure field. The deltas between both reported lift and drag as well as their components from the nominal values shown in Table 11 are shown in Table 13. Turning on the tangent jet in case 1 increases all lift components, and decreases drag slightly because the momentum thrust from the jet is greater than the increased pressure drag. Turning the normal jet on in case 2 increases lift twice as effectively as the tangent-jet-only configuration due to the massive amount of pressure lift provided, but also increases drag by roughly 9.5%. Though the tangent jet of the CRM-HL trade-off study is in a different flap chord location than in the NLR7301's trade-off study, its location serves the same relative purpose of energizing the separated suction-side boundary layer at the separation point. Thus, the deltas for case 3 are surprising, as they do not follow the trends of the corresponding case of the NLR7301 trade-off study (case 6). Here, both jets blowing at half strength cause the disadvantageous effect of drastically decreasing pressure lift despite decreasing pressure drag. Case 4 also has lift and drag deltas differing in trend from its corresponding case in the NLR7301 trade-off study (case 5). Here, the pressure lift is more similar to the sum of the individual jets, unlike the 2D case where the tandem jets of the same strength provide a lift somewhere in-between the individual jets' contributions. The drag components of case 4 all fall in-between the values of case 1 and 2.

Table 13. CRM-HL Jet Trade-off Study Lift and Drag Deltas

	ΔC_l	ΔC_{lp}	ΔC_{lv}	ΔC_{lm}	ΔC_d	ΔC_{dp}	ΔC_{dv}	ΔC_{dm}
Case 1	0.024326	0.023904	0.000012	0.000409	-0.000220	0.002490	-0.000054	-0.002705
Case 2	0.060902	0.059235	0.000039	0.001628	0.013770	0.011586	0.000066	0.002118
Case 3	-0.051765	-0.052936	0.000154	0.001018	-0.009239	-0.008638	-0.000307	-0.000294
Case 4	0.080143	0.078036	0.000070	0.002037	0.013000	0.013562	0.000025	-0.000587

The changes of lift and drag can be explained by looking at Figure 32, which shows C_{fx} and streamlines on the inboard flap suction side for each trade-off case. Looking at Figure 32, turning on the tangent jet in case 1 mostly reattaches the massive separation caused by the interaction of the nacelle wake and flap track fairing blockage, but doesn't fully reattach the small separations near the trailing edge due to its distance from them. In case 2, the Coanda effect of the normal jet fully reattaches the small trailing edge separation regions on the suction side of the flap, but doesn't effect the large separation because the flap track fairing blocks and diverts the jet's flow and thus its effect on the pressure field local to that separation. Case 3 shows that the small trailing edge separations have drastically grown in size due to the interaction of the

tandem weaker jets. These new separated regions cause a swirling pattern which lowers the pressure above the flap and reduces the pressure differential. Case 4 shows an additive effect of the individual jets seen in cases 1 and 2: the separation over the flap track fairing has been moderately re-attached, though to a lesser extent than case 1, and all the smaller inboard trailing edge separations have been re-attached as in case 2.

The large recirculation pattern present for case 3 in Figures 32(g) and 32(i) warrants further investigation due to how problematic it is from an aerodynamic perspective. Figure 33 shows a series of slices on and aft of the inboard flap depicting vorticity magnitude. A series of large vortex structures are clearly present upstream of the flap. A clear example view of these structures is seen in Figure 33(a). Two large vortex structures start from the nacelle pylon forward attachment and the chine located on the inboard part of the nacelle. Additionally, two inboard vortices start from the inboard slat trailing edge and its corresponding cut-out, and then merge. The vortex structures travel over the wing and interact with the inboard flow. Difference normal/tangent-blowing jet configurations of the trade-off study interact with these vortices in different ways leading to the various separation (and attachment) patterns on the suction side of the inboard flap. When the tangent-blowing jet is at full strength, it both overcomes the adverse pressure gradient present over the flap track fairing and is strong enough to entrain a pressurized flow underneath it on the further inboard sections of the flap. However, when the tangent-blowing jet is half strength, it acts as a blockage, mixing in the upstream vortex formations from the nacelle and slat with the boundary layer, fully detaching the flow and creating massive recirculation. A slice through the central separation in Figure 32(g) showing streamlines colored by C_p is shown for all trade-off study cases in Figure 34. Thus, this issue is preventable as long as the tangent blowing jet is strong enough.

Figure 35 shows C_p at slice locations A, B, and C (see Figure 26), and reinforces the flow separation trends seen in Figure 32. As stated previously, the large lower profile gap seen in slice C is where the flap track fairing is attached to the wing. For slices A and B, the tangent jet of case 1 induces very little shift in the baseline C_p profile except local to the jet. For slice C, it produces a profile which is almost a recovery of the baseline profile in slices A and B; a clear indication that the flow has been re-attached over most of the flap chord length. The slightly flatness of the case 1 profile near the trailing edge in slice C shows that there is still minor separation in that region, however. Case 2 shows the clear lifting of the suction-side and jet-local pressure-side C_p profiles due to the reasons discussed earlier in Section VII.A, but somewhat lowers the separated baseline profile seen for slice C. The case 3 profiles in slices A and B show the same high initial slope and subsequent plateau on the suction side of the flap as is seen for the non-case 1 profiles in slice C, indicating that case 3 is largely separated in all three slice locations. The case 4 profiles are similar to those of case 2 for slices A and B, and similar (though slightly lower on the suction side) to case 1 in slice C. This shows it has the beneficial effects of both individual jets, though at the cost of roughly twice the mass flow requirement.

VIII. Conclusion

This work explored how jet angle affects the performance and aerodynamic control capabilities of microjets. A boundary condition and consistent construction strategy was developed for implementing compressible, angled microjets on airfoils. Best practices for simulating the 2D NLR7301 and 3D CRM-HL HLPW4 airfoil systems with angled microjets were then determined for the LAVA code, and the angled jets placed on their flaps (inboard flap only for the CRM-HL) were verified against experimental data and CFD results where possible. Jets were placed on the pressure side of the flap at 95% of the flap chord, and on the suction side of the flap just upstream of separation onset. An exploration of calculation methods for angled jet parameters showed that the dominant influence on the airfoil system was the injected mass and momentum.

A series of studies were performed with the 2D NLR7301 geometry. A matrix of cases comparing the interdependence of angle and jet strength were performed, and determined that for a given flap deflection and free-stream condition there exists a range of jet angles for a given jet strength which approximate the effect of perfectly normal-blowing. The momentum component of drag was also found to significantly influence delta drag trends as it was on the same magnitude as the pressure and viscous components. Next an 'off-nominal' study was conduced, expanding the jet angle-strength matrix to include jet strengths which were much stronger than expected from a systems perspective. This study found that there are (highly unlikely) cases in which unique and detrimental aerodynamic effects arise from the insertion of microjets into an existing airfoil system, underlining that care must be taken during testing. It also showed that in 2D, the form of unsteadiness induced in the airfoil system can be characterized with lift standard deviation

magnitude. Finally, a jet trade-off study was performed on the NLR7301 in which a normal-blowing jet on flap's pressure side were compared to a more traditional tangent-blowing jet on the flap's suction side. This showed that for a single normal or tangent jet lift was increased and drag was decreased. If the strength of a single jet is split between both firing simultaneously then the lift gain and drag reduction fell somewhere between the individual jets, however if both jets were turned on at their original strength, the lift increase and drag decrease was slightly greater than either jet individually. A breakdown in vortex formation was also performed as part of this study for the various jet formations, and linked trends seen to physical phenomena within the system.

Two studies were performed with the 3D CRM-HL which corresponded to NLR7301 studies in order to explore the differences between 2D and 3D angled jet trends. A singled angled jet sweep was conduced for a jet on the pressure side of the flap. This showed a similar range of jet angles across which the effect of normal-blowing could be assumed from a lift delta perspective. However, unlike with the NLR7301, the pressure component of drag dominated the viscous and momentum components, meaning that this same normal-blowing-assumption jet angle range was also applicable to drag deltas. When looking at the separation pattern on the inboard flap, turning on the pressure jet reattached the flow near the trailing edge but did not affect the large separation above the flap track fairing. This trend was insensitive to jet angle, except when the jet was angled nearly tangent downstream (which removed the pressure field change normally caused by the blockage of the pressure-side jet shooting into the free-stream). Lastly, a trade-off study was performed for the CRM-HL which mimicked that of the NLR7301 (though the suction side jet was further upstream on the flap in order to precede the large separation over the flap track fairing). This study found that tangent-blowing reduced the large separation on the inboard flap, slightly increasing lift and drag, while normal-blowing reduced the small trailing edge separation regions on the flap, significantly increasing both lift and drag. When both jets were turned on in tandem at half strength, massive separations occurred which drastically reduced lift due to the induced mixing of the upstream vortex structures with the boundary layer. However, when both jets were turned on at full strength, separations on the trailing edge disappeared and the large separation over the flap track fairing was reduced, resulting in an even larger increase in lift, and slightly lower increase in drag than seen for the normal-jet only case.

In summary, implementation and exploration of angled microjets performed in this work has shown that there is clear leeway for jets to still have a 'normal-blowing' effect while being constrained by flap geometry requirements. While there were issues found for unusual or untested jet configurations - such as exceptionally strong upstream-pointing jets or having both pressure-side normal and suction-side tangent jets on at half strength - this simply underlines the need for robust design and flight testing.

Acknowledgments

This research has been funded by NASA's Advanced Air Transport Technology (AATT) project. Resources supporting this work were provided by the NASA High-End Computing (HEC) Program through the NASA Advanced Supercomputing (NAS) Division at Ames Research Center. The authors would like to thank and acknowledge Shishir A. Pandya (NASA ARC) and C. P. (Case) van Dam (UC Davis) for their knowledge of and insight into the active flow control field, as well internal review, Latunia P. Melton (NASA LaRC) for her leadership and insights, Leonardo M. Machado (NASA ARC) for internal review, Oliver M. F. Browne (NASA ARC) for visualization scripting advice, and Cetin C. Kiris for his guidance and leadership of the LAVA team.

References

[1]Nield, B. N., "An overview of the Boeing 777 high lift aerodynamic design," *Aeronautical Journal*, Vol. 99, 1995, pp. 361–371.

[2]Reckzeh, D., "Aerodynamic design of the high-lift-wing for a megaliner aircraft," *Aerospace Science and Technology*, Vol. 7, No. 2, 2003, pp. 107–119.

[3]Resende, O. C. D., "The evolution of the aerodynamic design tools and transport aircraft wings at Embraer," *Journal of the Brazilian Society of Mechanical Sciences and Engineering*, Vol. 26, No. 4, 2004, pp. 379–390.

[4]Meredith, P., "Viscous phenomena affecting high-lift systems and suggestions for future CFD development. High-lift System Aerodynamics," *AGARD CP*, Vol. 515, 1993, pp. 19(1)–19(8).

[5]Desalvo, M., Whalen, E., and Glezer, A., "High-lift enhancement using active flow control," 2012.

[6]Petz, R. and Nitsche, W., "Active control of flow seperation on a swept constant chord half model in a high-lift configuration," 2006.

[7]DeSalvo, M., Gissen, A., Whalen, E., and Glezer, A., "High-lift performance enhancement of a simple flap using aerodynamic flow control," 2016.

[8]Englar, R. and Huson, G., "Development of advanced circulation control wing high-lift airfoils," *Journal of Aircraft*, Vol. 21, No. 7, 1984, pp. 476–483.

[9]Jones, G., Viken, S., Washburn, A., Jenkins, L., and Cagle, C., "An active flow circulation controlled flap concept for general aviation aircraft applications," 2002.

[10]Jensch, C., Pfingsten, K., Radespiel, R., Schuermann, M., Haupt, M., and Bauss, S., "Design aspects of a gapless high-lift system with active blowing," 2009.

[11]Malavard, L., Poisson-Quinton, P., and Jousserandot, P., "Theoretical and experimental investigations of circulation control," Tech. rep., Princeton University Department of Aeronautical Engineering, 1956.

[12]Boeije, C., de Vries, H., Cleine, I., van Emden, E., Zwart, G., Stobbe, H., Hirschberg, A., and Hoeijmakers, H., "Fluidic Load Control for Wind Turbine Blades," 2009.

[13]Traub, L. and Agarwal, G., "Aerodynamic Characteristics of a Gurney/Jet Flap at Low Reynolds Numbers," *Journal of Aircraft*, Vol. 45, No. 2, 2008, pp. 424–429.

[14]Cooperman, A., *Wind Tunnel Testing of Microtabs and Microjets for Active Load Control of Wind Turbine Blades*, Ph.D. thesis, Univ. of California, Davis, CA, 2012.

[15]Blaylock, M., Chow, R., Cooperman, A., and van Dam, C., "Comparison of Pneumatic Jets and Tabs for Active Aerodynamic Load Control," *Wind Energy*, Vol. 17, No. 9, 2014, pp. 1365–1384.

[16]Cruz, J. and Anders, A., "Assessment of an Unstructured-Grid Method for Predicting Aerodynamic Performance of Jet Flaps," 2006.

[17]Poisson-Quinton, P. and Lepage, L., *Survey of French Research on the Control of Boundary Layer and Circulation*, Vol. 1, Pergamon Press, New York, 1961.

[18]Blaylock, M., Chow, R., and van Dam, C., "Comparison of Microjets with Microtabs for Active Aerodynamic Load Control," 2010.

[19]Brunner, M., Blaylock, M., Cooperman, A., and van Dam, C., "Comparison of CFD with Wind Tunnel Tests of Microjets for Active Aerodynamic Load Control," 2012.

[20]Traub, L., Miller, A., and Rediniotis, O., "Comparisons of a Gurney and Jet-Flap for Hinge-Less Control," *Journal of Aircraft*, Vol. 41, No. 2, 2004, pp. 420–423.

[21]D.J. Heathcote, e. a., "Control of Wing Loads by means of Blowing and Mini-Tabs," 2015.

[22]Hosseini, S., van Dam, C., and Pandya, S., "Computational investigation of nominally-orthogonal pneumatic active flow control for high-lift systems," 2018.

[23]Hosseini, S., Cooperman, A., Dam, C. V., and Pandya, S., "Microjet Configuration Sensitivities for Lift Enhancement in High-Lift Systems," 2019.

[24]Hosseini, S., Cooperman, A., Dam, C. V., and Pandya, S., "Microjets for lift enhancement and separation mitigation in high-lift systems," 2019.

[25]Hosseini, S., van Dam, C., and Pandya, S., "Aerodynamic load control for multi-element airfoils using surface-normal trialing-edge blowing," *Journal of Aircraft*, Vol. 56, No. 4, 2019, pp. 1668–1676.

[26]Johnson, S. J., Baker, J. P., van Dam, C. P., and Berg, D., "An overview of active load control techniques for wind turbines with an emphasis on microtabs," *Wind Energy*, Vol. 13, 2010, pp. 239–253.

[27]Vandenberg, B. and Oskam, B., "Boundary layer measurements on a two-dimensional wing with flap and a comparison with calculations," 1980.

[28]Lin, J. C., Melton, L. G. P., Viken, S., Andino, M. Y., Koklu, M., Hannon, J., and Vatsa, V. N., "High Lift Common Research Model for Wind Tunnel Testing: An Active Flow Control Perspective," *55th AIAA Aerospace Sciences Meeting*, AIAA, 2017.

[29]Jensen, J. C., Stich, G.-D., Housman, J. A., Denison, M., and Kiris, C. C., "LAVA Simulations for the 3rd AIAA CFD High Lift Prediction Workshop using Body Fitted Grids," *AIAA Scitech 2018 Forum*, AIAA, 2018.

[30]Hosseini, S., Dam, C. V., and Pandya, S., "Surface-Normal Active Flow Control for Lift Enhancement and Separation Mitigation for High-Lift Common Research Model," 2021.

[31]Duensing, J. C., Housman, J. A., Fernandes, L. S., Machado, L. G., and Kiris, C. C., "A Reynolds-Averaged Navier-Stokes Perspective for the High Lift-Common Research Model Using the LAVA Framework," *AIAA Aviation 2022 Forum*, AIAA, 2022.

[32]Kiris, C. C., Barad, M. F., Housman, J. A., Sozer, E., Brehm, C., and Moini-Yekta, S., "The LAVA Computational Fluid Dynamics Solver," *52nd AIAA Aerospace Sciences Meeting*, No. 0070, AIAA, 2014.

[33]Kiris, C. C., Housman, J. A., Barad, M. F., Brehm, C., Sozer, E., and Moini-Yekta, S., "Computational Framework for Launch, Ascent, and Vehicle Aerodynamics (LAVA)," *Aerospace Science and Technology*, Vol. 55, Aug. 2016, pp. 189–219.

[34]Chan, W. M., "Developments in Strategies and Software Tools for Overset Structured Grid Generation and Connectivity," *20th AIAA Computational Fluid Dynamics Conference*, No. 3051, AIAA, 2011.

[35]Kenway, G. K. W., Secco, N., Martins, J. R. R. A., Mishra, A., and Duraisamy, K., "An Efficient Parallel Overset Method for Aerodynamic Shape Optimization," *58th AIAA/ASCE/AHS/ASC Structures, Structural Dynamics, and Materials Conference*, No. 0357, AIAA, 2017.

[36]Saad, Y. and Schultz, M. H., "GMRES: A generalized minimal residual algorithm for solving nonsymmetric linear systems," *SIAM Journal on scientific and statistical computing*, Vol. 7, No. 3, 1986, pp. 856–869.

[37]Destarac, D., "Spurious Far-Field-Boundary Induced Drag in Two-Dimensional Flow Simulations," *Journal of Aircraft*, Vol. 48, No. 4, 2011, pp. 1444–1455.

[38]Housman, J. A., Kiris, C. C., and Hafez, M. M., "Time-Derivative Preconditioning Methods for Multicomponent Flows—Part I: Riemann Problems," *Journal of Applied Mathematics*, Vol. 76, No. 2, Feb. 2009.

[39]Housman, J. A., Kiris, C. C., and Hafez, M. M., "Time-Derivative Preconditioning Methods for Multicomponent Flows—Part II: Two-Dimensional Applications," *Journal of Applied Mathematics*, Vol. 76, No. 2, March 2009.

[40]Spalart, P. and Allmaras, S., "A One-Equation Turbulence Model for Aerodynamic Flows," *30th Aerospace Sciences Meeting and Exhibit*, No. 0439, AIAA, 1992.

[41]Shur, M. L., Strelets, M. K., Travin, A. K., and Spalart, P. R., "Turbulence Modeling in Rotating and Curved Channels: Assessing the Spalart-Shur Correction," *AIAA Journal*, Vol. 38, No. 5, 2000, pp. 784–792.

[42]Spalart, P. R., "Strategies for Turbulence Modeling Simulations," *International Journal of Heat and Fluid Flow*, Vol. 21, 2000, pp. 252–263.

[43]Menter, F., "Two-Equation Eddy-Viscosity Turbulence Models for Engineering Applications," *AIAA Journal*, Vol. 32, No. 8, 1994, pp. 1598–1605.

[44]Hosseini, S., Cooperman, A., van Dam, C., and Pandya, S., "Microjet Configuration Sensitivities for Active Flow Control on Multi-Element High-Lift Systems," *Journal of Aircraft*, Vol. 58, No. 4, 2021, pp. 1–19.

[45]Rumsey, C. L., Slotnick, J. P., Long, M., Stuever, R., and Wayman, T., "Overview and Summary of the First AIAA High Lift Prediction Workshop," *Journal of Aircraft*, Vol. 48, No. 6, 2011, pp. 2068–2079.

[46]Rumsey, C. L., Slotnick, J. P., Long, M., Stuever, R., and Wayman, T., "Overview and Summary of the Second AIAA High Lift Prediction Workshop," *Journal of Aircraft*, Vol. 52, No. 4, 2015, pp. 1006–1025.

[47]Rumsey, C. L., Slotnick, J. P., and Sclafani, A. J., "Overview and Summary of the Third AIAA High Lift Prediction Workshop," *Journal of Aircraft*, Vol. 56, No. 2, 2019, pp. 621–644.

[48]Rumsey, C. L., Slotnick, J. P., and Woeber, C. D., "Overview and Summary of the Fourth AIAA High Lift Prediction Workshop," *Journal of Aircraft (Article in Advance)*, Vol. 60, No. 2, 2023, pp. 1–18.

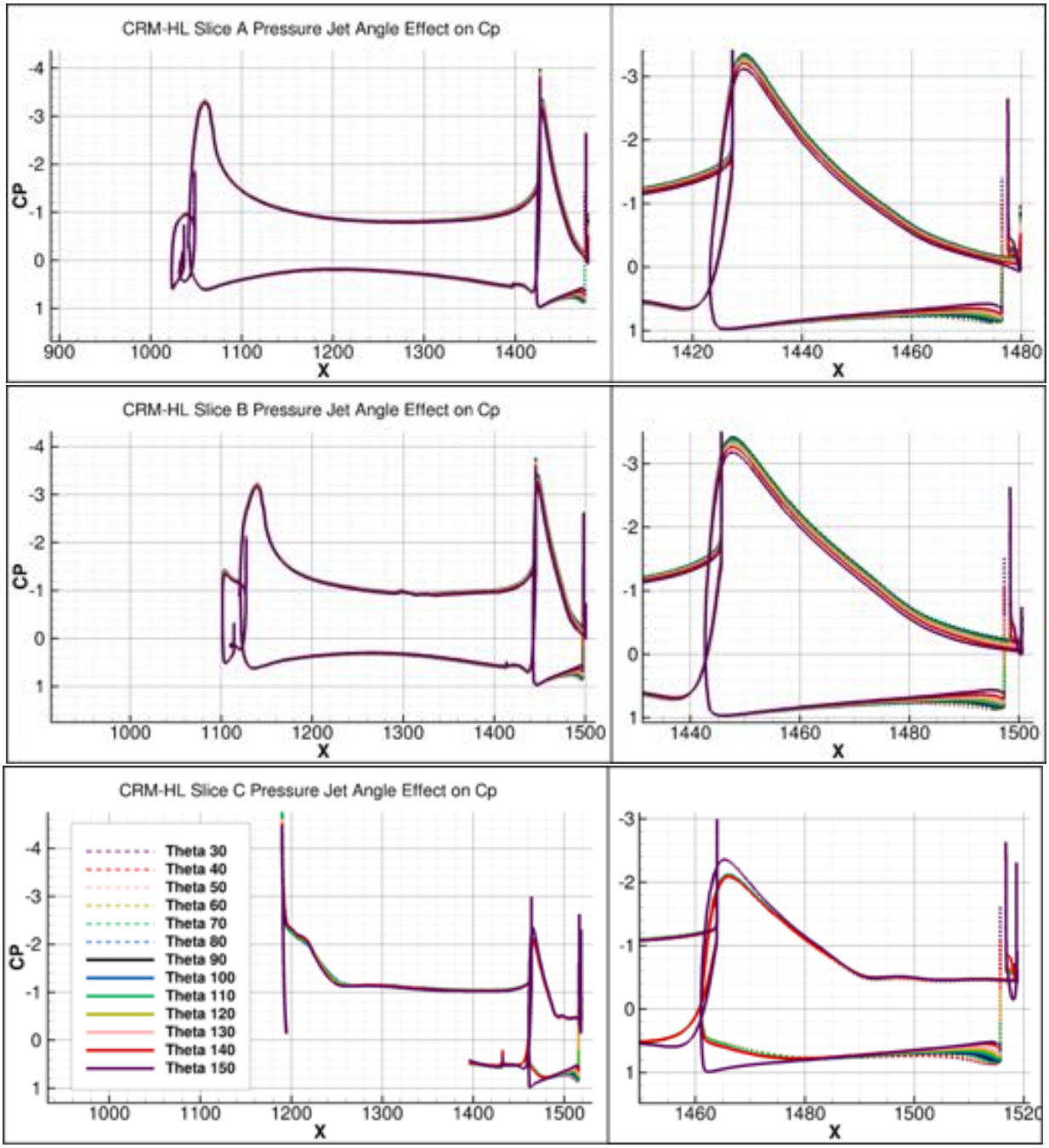

Figure 30. Coefficient of pressure C_p for each θ_{jet} in the constant $C_{\mu,jet}$ sweep extracted from the CRM-HL slat, wing, and inboard flap at slice locations A (*Top*), B (*Center*), and C (*Bottom*), as shown in Figure 26. (*Left*): full slat+wing+flap. (*Right*): closeup on flap. x is in inches.

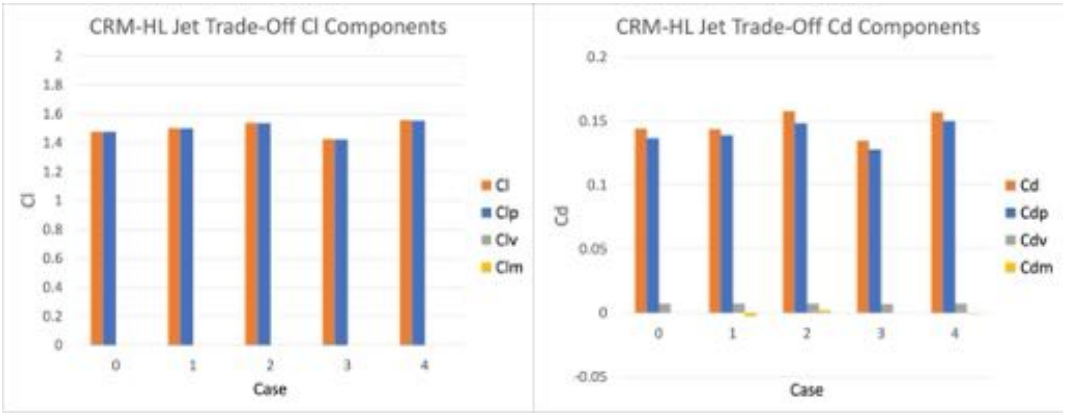

Figure 31. CRM-HL delta lift and drag (ΔC_l and ΔC_d) values for the jet trade-off study. Pressure component dominates viscous and momentum components in all cases.

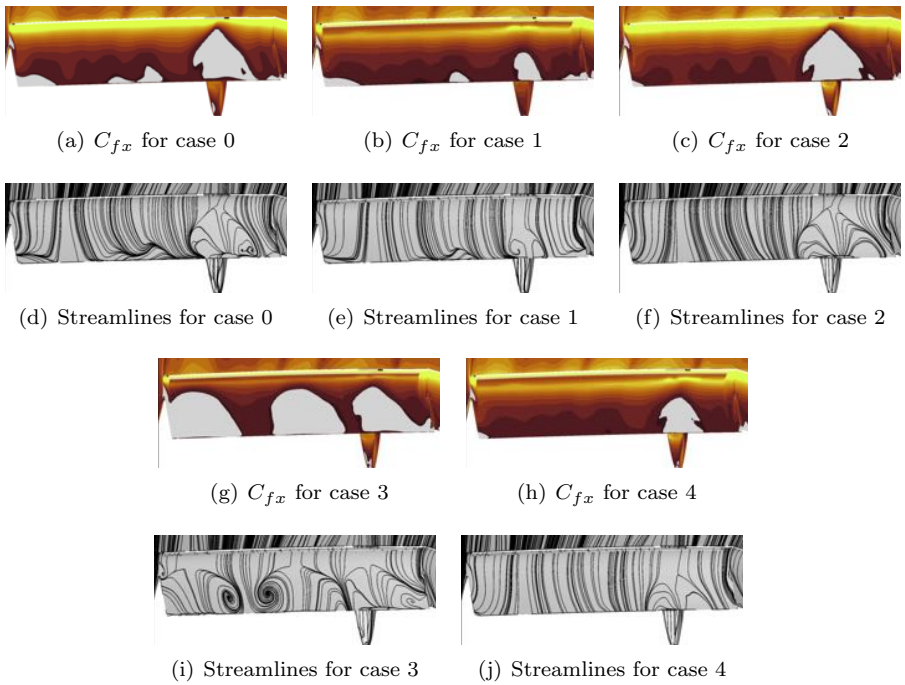

(a) C_{fx} for case 0 (b) C_{fx} for case 1 (c) C_{fx} for case 2

(d) Streamlines for case 0 (e) Streamlines for case 1 (f) Streamlines for case 2

(g) C_{fx} for case 3 (h) C_{fx} for case 4

(i) Streamlines for case 3 (j) Streamlines for case 4

Figure 32. CRM-HL inboard flap suction-side surface C_{fx} and streamlines for the trade-off study. C_{fx} has a cutoff below zero marking recirculation zones.

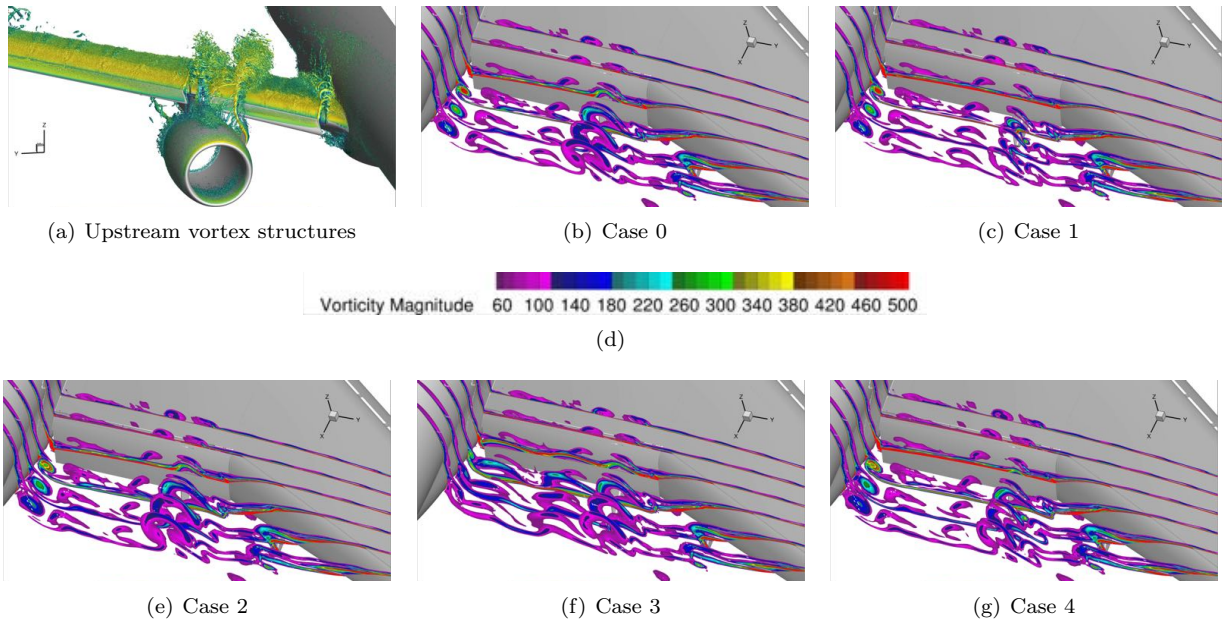

(a) Upstream vortex structures (b) Case 0 (c) Case 1

(d)

(e) Case 2 (f) Case 3 (g) Case 4

Figure 33. Formation of and interaction with CRM-HL leading edge vortex structures and the microjets of the trade-off study. Sub-figure 33(a) is from a separate body of work in which a wall-modeled large eddy simulation was performed on the CRM-HL over a large angle of attack sweep. Near the $C_{l,max}$ of 18° an isocontour of Q-criteria colored by normalized x-direction velocity is plotted to illustrate common flow features relevant to the CRM-HL trade-off study performed in this work.

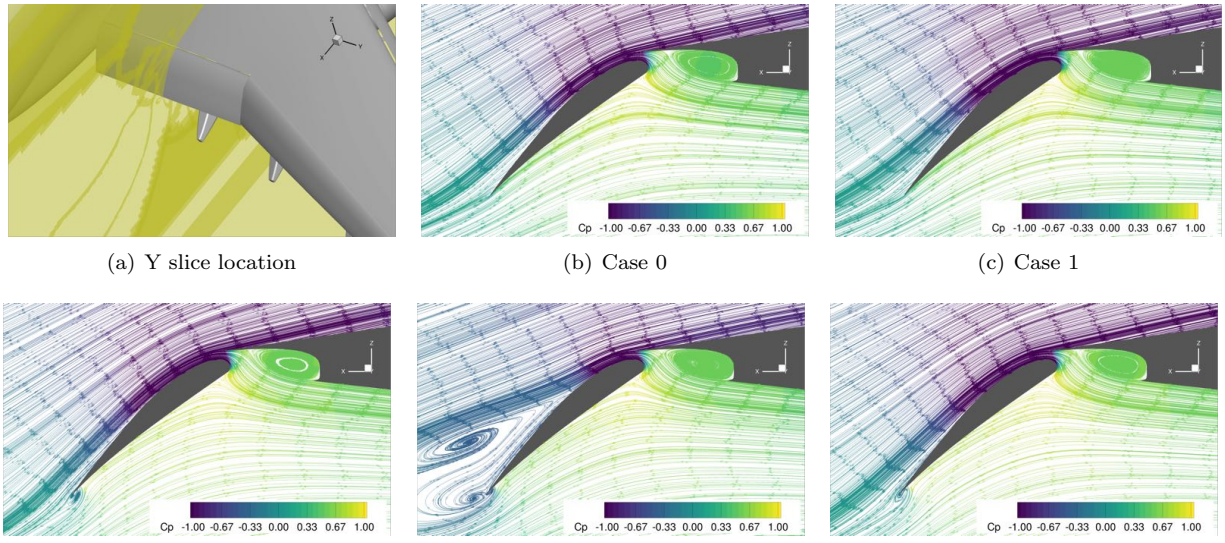

(a) Y slice location (b) Case 0 (c) Case 1

(d) Case 2 (e) Case 3 (f) Case 4

Figure 34. Y slices across the wing and flap for the cases of the CRM-HL trade-off study. Streamlines are colored by C_p.

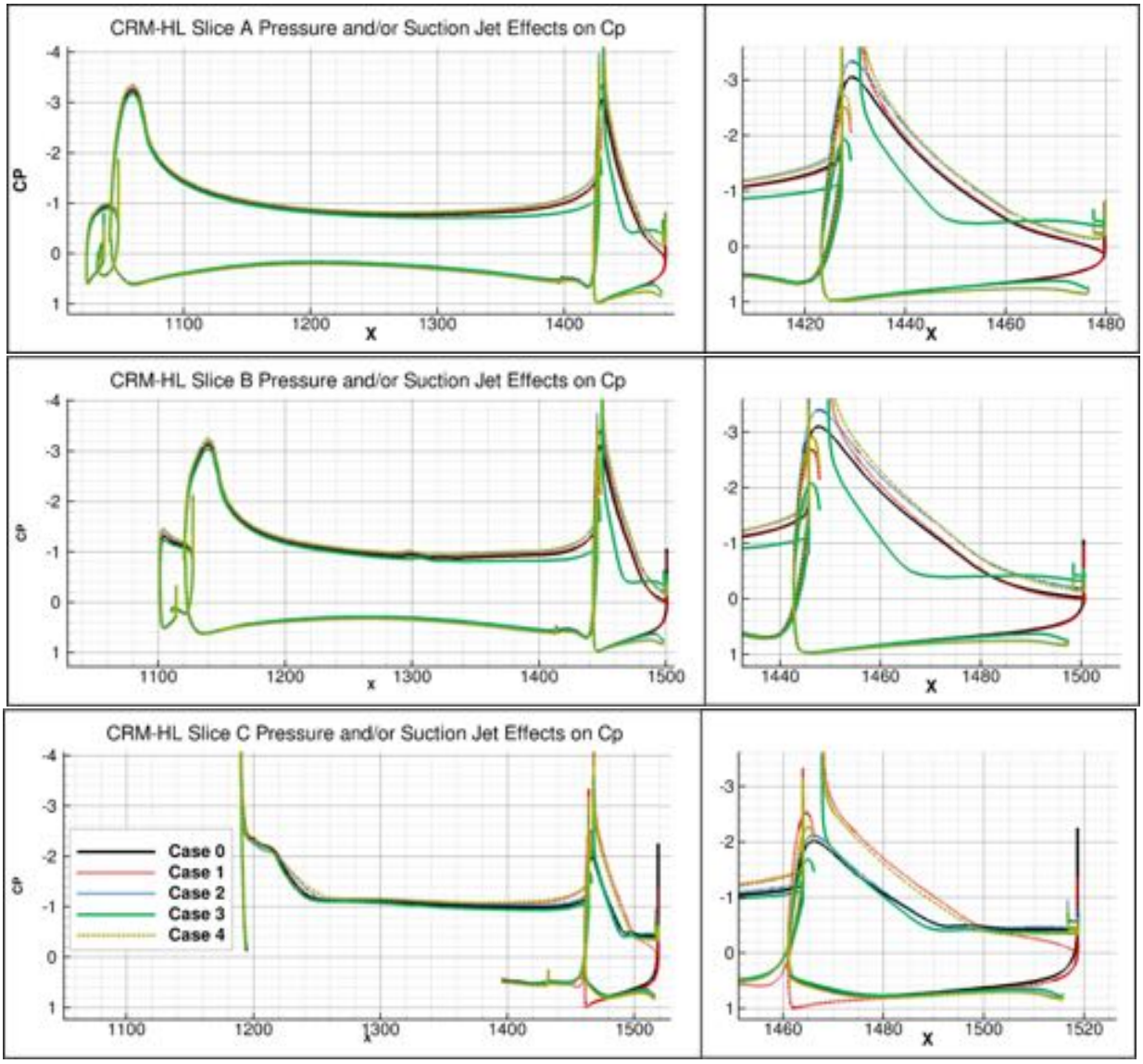

Figure 35. Coefficient of pressure C_p for each case of the CRM-HL jet trade-off study at slice locations A (*Top*), B (*Center*), and C (*Bottom*), as shown in Figure 26. (*Left*): full slat+wing+flap. (*Right*): closeup on flap. x is in inches.